Aerosol Res., 3, 477–502, 2025 https://doi.org/10.5194/ar-3-477-2025 © Author(s) 2025. This work is distributed under the Creative Commons Attribution 4.0 License.





AIDA Arctic transport experiment – Part 1: Simulation of northward transport and aging effect on fundamental black carbon properties

Marco Zanatta^{1,2}, Pia Bogert¹, Patrick Ginot³, Yiwei Gong^{1,a}, Gholam Ali Hoshyaripour⁴, Yaqiong Hu¹, Feng Jiang^{1,b}, Paolo Laj^{3,c}, Yanxia Li¹, Claudia Linke¹, Ottmar Möhler¹, Harald Saathoff¹, Martin Schnaiter^{1,d}, Nsikanabasi Silas Umo^{1,e}, Franziska Vogel^{1,f}, and Robert Wagner¹

¹Institute of Meteorology and Climate Research – Atmospheric Aerosol Research,
Karlsruhe Institute of Technology, Karlsruhe, Germany

²Institute of Atmospheric Science and Climate, National Research Council of Italy, Bologna, Italy

³University Grenoble Alpes, CNRS, IRD, G-INP, Institut des
Géosciences de l'Environnement, Grenoble, France

⁴Institute of Meteorology and Climate Research Troposphere Research,
Karlsruhe Institute of Technology, Karlsruhe, Germany

^anow at: PSI Center for Energy and Environmental Sciences, 5232 Villigen PSI, Switzerland

^bnow at: School of Public and Environmental Affairs, Indiana University, Bloomington, IN 47401-2204, USA

^cnow at: World Meteorological Organization, Geneva, Switzerland

^dnow at: Institute for Atmospheric Research of Wuppertal, Wuppertal, Germany

^enow at: Department of Chemistry and Biochemistry, University of North Carolina Wilmington,
Wilmington, North Carolina 28403, USA

^fnow at: Institute of Atmospheric Science and Climate, National Research Council of Italy, Bologna, Italy

Correspondence: Marco Zanatta (m.zanatta@isac.cnr.it) and Gholam Ali Hoshyaripour (gholamali.hoshyaripour@kit.edu)

Received: 18 March 2025 – Discussion started: 9 April 2025 Revised: 1 August 2025 – Accepted: 28 August 2025 – Published: 3 November 2025

Abstract. Black carbon (BC) is a key atmospheric forcer due to its interaction with solar radiation and clouds. However, accurately quantifying and understanding the impact of atmospheric aging on BC properties and radiative forcing remains a major challenge. To address this, the AIDA (Atmospheric Interactions and Dynamics in the Atmosphere) aRCtic Transport Experiment (ARCTEx) project simulated BC aging under quasi-realistic Arctic conditions in the AIDA chamber. Four distinct scenarios were simulated based on reanalysis data, representing summer and winter conditions at both low and high altitudes, to capture the variability in BC aging processes in the presence of nitrate and organic matter precursors during Arctic transport.

In the first part of the paper, we define the meteorological conditions characterizing northward transport under different scenarios and describe the technical solutions to simulate 5 d transport in the AIDA chamber. In the second part of the work, we assess the evolution of fundamental properties, including density, morphology, and mixing state, as observed during the aging process.

The ARCTEx project demonstrates that large facilities such as AIDA can successfully reproduce environmental conditions, enabling a gradual aging process that closely follows the natural timescales observed in the atmosphere. Our experiments revealed that temperature strongly influences the aging timescale and the evolution of BC's diameter, effective density, and coating thickness. Low-altitude scenarios exhibited rapid aging, resulting in fully coated, compact BC particles within 39–98 h, corresponding to 50 and 80° N, respectively. In contrast, high-altitude transport was characterized by slow aging, with limited coating and compaction, even after 115 h of simulation. These findings provide valuable insights into the temporal evolution of BC properties during Arctic

transport. In forthcoming work, we will report the implications of this evolution for climate-relevant properties such as light absorption and activation as cloud droplets and ice crystals. Together, these studies aim to enhance the representation of BC aging in climate models, reducing uncertainties in Arctic radiative-forcing estimates.

1 Introduction

Black carbon (BC) is a primary carbonaceous aerosol emitted by combustion processes. Due to its strong absorption of visible light, BC is the only aerosol that exerts a net warming effect (IPCC, 2023). As described by Schulz et al. (2006), the direct radiative forcing of BC is proportional to its mass absorption cross-section (MAC) and its atmospheric lifetime. While MAC quantifies the amount of light absorbed per unit mass of BC, the lifetime depends on BC's ability to act as cloud condensation nuclei (CCN) and ice-nucleating particles (INPs). These three climate-relevant properties (MAC, CCN, and INPs) are directly influenced by BC's fundamental physical and chemical characteristics, including particle diameter, mixing state, and morphology (Bond et al., 2013). However, these properties vary during the lifetime of BC due to atmospheric aging. Consequently, the radiative forcing of BC also varies as a function of its atmospheric age. As summarized by Li et al. (2024b), mixing with other chemical substances can enhance BC's net light absorption and increase its hygroscopicity. However, significant uncertainties remain: (i) the magnitude of absorption enhancement is still debated (Cappa et al., 2012), (ii) closure studies are not yet robust enough to confirm BC's role as a CCN (Bond et al., 2013), and (iii) BC's freezing efficiency in cirrus clouds is still unclear (Burrows et al., 2022).

Considering the long lifetime of BC in the Arctic (5.5 d; Lund et al., 2018), the impact of aging on the evolution of BC's fundamental and climate-relevant properties during Arctic long-range transport remains challenging to reproduce in global models (Lund and Berntsen, 2012; Mahmood et al., 2016). This generates significant uncertainties in the estimation of BC concentrations and radiative forcing in the Arctic region (Samset et al., 2013). Moreover, the limited observational capability of aging-induced modification of BC does not allow us to fully validate the performances of global models (Samset et al., 2018). In fact, most measurements in the Arctic provide only static snapshots of BC properties, offering limited insight into the dynamic processes that occur during the transport and lead to internal mixing (Kodros et al., 2018), absorption enhancement (Zanatta et al., 2018), and cloud activation (Zanatta et al., 2023; Zieger et al., 2023) in the Arctic region.

On the other hand, experiments conducted in laboratory setups using flow tubes and simulation chambers have been essential in advancing our understanding of the aging processes of aerosol and black carbon particles (Doussin et al., 2023). In general, these studies reported a significant mod-

ification of BC properties as a function of chemical and physical aging, including morphology (e.g., Saathoff et al., 2003a; Corbin et al., 2023), light absorption (e.g., Schnaiter et al., 2005; Fierce et al., 2020), hygroscopicity (e.g., Henning et al., 2012; Dalirian et al., 2018; Friebel and Mensah, 2019), and ice nucleation activity (e.g., Möhler et al., 2003; Kanji et al., 2020). Although chamber experiments on BC aging have been actively implemented to constrain global models (Wang et al., 2018), they are often conducted under controlled conditions that may not fully represent realworld atmospheric environments. These experiments typically involve high concentrations; short timescales; and limited variability in temperature, humidity, and chemical composition. As a result, aging processes may occur with different timescales and effects compared to ambient atmospheric conditions, introducing challenges in translating experimental findings into model parameterizations. Improving the representation of BC aging in models is crucial for reducing uncertainties in climate projections as accurate simulations of BC properties and evolution are essential for assessing its radiative forcing and cloud interactions (Wang et al., 2018).

BC variability in the Arctic was often associated with co-emitted sulfate aerosol from anthropogenic sources (e.g., Massling et al., 2015) and organic aerosol from biomass burning events (e.g., Moschos et al., 2022), while its correlation with nitrate was mostly ignored (AMAP, 2021). Similarly, chamber studies focused on the evolution of BC properties as function of internal mixing with sulfate (e.g., Möhler et al., 2005; Khalizov et al., 2009; Henning et al., 2012) and organics (e.g., Lefevre et al., 2019; Wittbom et al., 2014). As a consequence, the impact of BC-nitrate internal mixing on fundamental and climate-relevant properties remained poorly assessed (Yuan et al., 2020). Internal mixing of BC with nitrate species has become particularly important in the Arctic region, where nitrate aerosol concentration has been increasing since the 1980s despite an overall reduction in nitrogen oxide emissions (AMAP, 2021). The same report underlined how few studies had focused on nitrate aerosol in the Arctic, introducing a knowledge gap regarding the sources of its precursors, its formation mechanisms, and its interaction with other atmospheric species such as BC.

ARCTEX (AIDA aRCtic Transport Experiment) was designed to reproduce, in the AIDA (Aerosol Interaction and Dynamics in the Atmosphere) chamber, the meteorological and chemical conditions that BC undergoes during Arctic transport, focusing on mixing with nitrogen-based species. By simulating different transport scenarios, we aim to understand and quantify the aging timescale and the impacts

on fundamental and climatic-relevant properties of BC during different seasons and at different altitudes. In the present work, we present the proof of concept of ARCTEx, including the definition of Arctic transport conditions; a full technical description of the unprecedented 5 d long experiments; and the evolution of fundamental properties such as diameter, density, morphology, and mixing state. A second publication will aim to explore the relationship of the aging timescale explored here with climate-relevant properties.

2 Methods

The objective of ARCTEx is to quantify the impact of aging on BC's fundamental and climate-relevant properties during long-range transport from mid-latitudes to the Arctic. This is achieved through chamber simulation experiments. The methodology section is structured as follows: first, we describe the identification of Arctic transport scenarios (Sect. 2.1) to be reproduced in the Aerosol Interaction and Dynamics in the Atmosphere (AIDA) chamber (Sect. 2.2). The procedures for injecting and measuring reactive gases and aerosol particles are detailed in Sect. 2.3 and 2.4, respectively. Finally, an overview of the experimental design and schedule is provided in Sect. 2.5.

2.1 Identification of Arctic transport scenarios

2.1.1 Region of interest

Aerosol particles can be transported from mid-latitudes to the Arctic region following various paths. As summarized in the AMAP report 2015 (Quinn et al., 2015), the transport of pollution is regulated by the seasonal variability of the "Arctic front" (Barrie, 1986), which controls the geographical origin of pollution and the altitude of the transport pathway. The Eurasian sector is a significant corridor for northward transport, and it is of particular interest to the member and observer countries of the Arctic Council due to very high BC emissions (Schacht et al., 2019). This sector is associated with intense export of anthropogenic (Backman et al., 2021) and natural (McCarty et al., 2021) black carbon emissions. Although other efficient transport patterns exist, the continental Eurasian sector is characterized by a reduced temperature variability (Przybylak, 2016), ensuring more homogeneous atmospheric conditions compared to the Atlantic and Pacific transport pathways. This uniformity is critical for the design of chamber experiments as it minimizes external variability and facilitates the representation of the ambient conditions, thereby reducing the operational complexity of the AIDA chamber. Hence, we identified the area of interest for ARCTEx in the Eurasian sector to be between 40 and 90° N latitude and between 60 and 140° E longitude (Fig. 1).

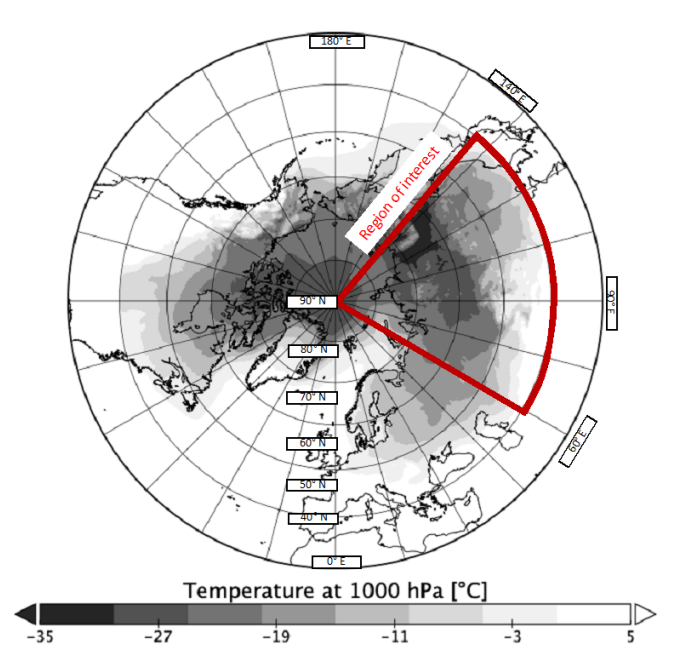


Figure 1. Global variability of atmospheric temperature at 1000 hPa as extracted from ERA5 monthly averaged data (mean of the year 2010). Marked in red is the region of interest for the ARCTEx project, limited to between 40–90° N and 60–140° E.

2.1.2 Transport pathways

In winter and early spring, the southern extent of the polar front (around 40° N) enables the rapid transport of pollution emitted from mid-latitudes in the Eurasian and North American regions to the lower troposphere of the Arctic. In summer, warm air masses from south of the Arctic front can move northward, maintaining a constant potential temperature. As they rise, these air masses reach the Arctic in the middle and upper troposphere but over a longer timescale compared to the faster winter transport. This seasonal variability results in a clear seasonality of BC concentration, with higher values in the winter-spring and lower ones in summer across the low and middle troposphere (Jurányi et al., 2023). In this work, January and July were assumed to be representative of the winter and summer seasons. In terms of altitude, we assumed 1000-800 hPa of atmospheric pressure to be representative of low altitudes (low troposphere) and 600-400 hPa atmospheric pressure to be representative of high altitudes (middle troposphere).

Overall, we recognized four distinct transport scenarios:

- summer (July) low-altitude (1000–800 hPa) transport (SL)
- winter (January) low-altitude (1000–800 hPa) transport (WL)
- summer (July) high-altitude (600–400 hPa) transport (SH)

 winter (January) high-altitude (600–400 hPa) transport (WH).

For these scenarios, we defined the northward-transport conditions within the region of interest as the latitudinal variability of meteorological and chemical properties experienced by a hypothetical air mass traveling from 40 to 90° N over a 5 d period. This variability was parameterized into a latitudinal profile, divided into five bins, each representing 10° of northward motion, equivalent to 1 d of suspension time.

2.1.3 Meteorological conditions

Temperature (T) and relative humidity (RH) data were extracted from the ERA5 monthly averaged data on pressure levels for the period between 2010 and 2020 and geographically limited to the region of interest. These global georeferenced reanalysis data are available with a $0.25^{\circ} \times 0.25^{\circ}$ horizontal resolution and a pressure range of 1000-1 hPa, binned in 37 pressure levels. A detailed description of the ERA5 products is provided by Hersbach et al. (2020). The median of T and RH was calculated for the low-altitude scenarios from the ERA5 pressure levels of 1000-950-900-850-800 hPa and for the high-altitude scenarios from the ERA5 pressure levels of 600-550-500-450-400 hPa. The mean georeferenced data in the two altitude levels were then organized into one longitudinal bin and five equally spaced latitudinal bins with a width of 10° N. Each bin represents the median of the $0.25^{\circ} \times 0.25^{\circ}$ grid in the corresponding altitude and longitude range described before. Daytime and nighttime dramatically change from winter to summer as a function of latitude (Table S1 in the Supplement). For the winter ARCTEx simulations (WL and WH), we assumed a decrease in daily light duration from 8 h on day 1 (40- 50° N) to 0 h on day 5 (80–90° N). For the summer ARC-TEx simulations (SL and SH), we assumed an increase in daily light duration from 16 h on day 1 (40-50° N) to 24 h on day 5 (80-90° N). Despite uncertainties, ERA5 temperature data show good agreement with in situ Arctic observations, with deviations of within 6% latitudinally (Pernov et al., 2024) and ~ 1 °C vertically (Graham et al., 2019), supporting its suitability for driving the ARCTEx experimental design. However, the $\sim 40\%$ underestimation of RH suggests limitations in replicating Arctic humidity conditions (Pernov et al., 2024), which may impact the representation of aerosol-phase processes in the chamber.

2.1.4 Atmospheric composition

While the source and origin of Arctic BC were often investigated with the variability of sulfate aerosol (Massling et al., 2015), the source partitioning and emission region of nitrate are rarely investigated in the Arctic (Moschos et al., 2022). Over the last few decades, considering the increase in the concentration of nitrate in the last few years compared to that of other inorganic atmospheric species (Zare et al.,

2018), nitrogen oxides and nitrate matter might represent, in the future, a non-negligible source for BC coatings. Hence, during ARCTEx, nitrogen dioxide (NO₂) was chosen as a major precursor to form an inorganic coating over BC. To investigate the nitrate coating formation, NO2 and BC mixing ratios were extracted from the CAMS (Copernicus Atmosphere Monitoring Service) dataset. These global georeferenced reanalysis data (fourth-generation ECMWF global reanalysis; EAC5) are available with a $0.75^{\circ} \times 0.75^{\circ}$ horizontal resolution and a pressure range of 1000-1 hPa, binned in 25 pressure levels. An overview of the CAMS products is provided by Inness et al. (2019), while details on the aerosol schemes are given in Morcrette et al. (2009) and Bozzo et al. (2017). The representativity of CAMS for Arctic conditions is poorly addressed. However, the NO₂ / BC ratio may be particularly uncertain due to seasonal underestimations of NO₂ and an oversimplified treatment of BC's hydrophilic conversion, which may impact transport and removal processes in the CAMS scheme (Ryu and Min, 2021; Ding and Liu, 2022). Despite these limitations, CAMS reliably captures large-scale trends and variability, making it a valuable dataset for our experimental design.

In light of the different conditions between the real atmosphere and a simulation chamber, we did not consider the absolute concentration of BC and NO2 but focused on the mass ratio of NO₂ over BC (NO₂ / BC). While NO₂ is a direct CAMS product, the ARCTEx BC mass concentration was calculated as the sum of the hydrophilic and hydrophobic components of BC provided by CAMS (Li et al., 2024a). Hence, in our analysis, BC was treated as a single component without distinguishing the hydrophilic and hydrophobic fractions. The NO₂ / BC mass ratio was calculated based on the same pressure levels and region of interest as the ERA5 data described above. The resulting latitude profiles of the NO₂ / BC ratio are listed in Table S1. Although ozone is an essential reactive component in the atmospheric nitrogen chemistry, it was not extracted from CAMS reanalysis data. To simplify the chamber operation, ozone was kept in excess with respect to NO₂ without respecting ambient variability. It must be noted that volatile organic compounds, which are a byproduct of combustion, were simultaneously emitted with BC and injected into the AIDA chamber without active control. As a result, the organic aerosol content in AIDA reflects the specific emissions of the burner and not ambientlike conditions. Therefore, although the experiments primarily targeted the evolution of BC mixing with nitrate coatings, the presence of organic vapors may interact or compete with NO₂ during condensation and coating formation, introducing additional complexity into the aging dynamics.

2.2 The AIDA aerosol and cloud simulation chamber

The ARCTEx experiments were conducted in July 2022 in the Aerosol Interaction and Dynamics in the Atmosphere (AIDA) chamber at the Karlsruhe Institute of Technology. The chamber has been described in detail in previous works (e.g., Möhler et al., 2003; Saathoff et al., 2003b; Vogel, 2022). Briefly, the AIDA chamber is a cylindrical aluminum vessel with a total volume of 84 m³, equipped with pressure, temperature, humidity, and light control systems. A simplified schematic of the AIDA facility and the instrumental setup is shown in Fig. 2. A flow of dry, particle-free synthetic air was continuously injected into the AIDA chamber to compensate for the sampling flow rate and to keep it at an overpressure of +1 hPa with respect to ambient conditions. The AIDA chamber is enclosed within a thermal housing, where heat exchangers control the air temperature, maintaining it at 60 to -90 °C. The chamber gas temperature was monitored with 24 fast-responding thermocouples oriented in the AIDA chamber volume on vertical and horizontal lines. A mixing fan, positioned 1 m above the bottom of the vessel, ensured that the temperature, gas, and aerosol particles were homogeneously mixed within 90 s at all times. Water vapor is measured in situ by a tunable diode laser hygrometer (Fahey et al., 2014) and extractively by a dew point mirror hygrometer (MBW373LX, MBW Calibration Ltd.). Based on these measurements, in case of excessive dilution drying of the chamber, the RH was actively increased by injection of a flow of humidified synthetic air. AIDA is equipped with an LED light source a to mimic the solar spectrum between 300 and 530 nm wavelength (Vallon et al., 2022). Considering the fact that the emissions of the different LEDs change with temperature, the current of the LED arrays was adjusted with every change of temperature in the chamber to match the spectrum at +20 °C. The light source was turned on and off, thereby setting the virtual sunrise and sunset according to the latitude-dependent irradiation time listed in Table S1. Thanks to its capabilities, the AIDA chamber has been used to investigate a wide range of atmospheric processes including, among the most recent, formation (Gao et al., 2022) and light absorption (Jiang et al., 2024) of secondary organic aerosol, ice-nucleating abilities of porous organic aerosol (Wagner et al., 2024), inorganic salts (Bertozzi et al., 2021) and volcanic ashes (Umo et al., 2021), and homogeneous freezing of sulfuric acid (Schneider et al., 2021)

2.3 Injection and measurement techniques of trace gases

Besides reactive gases, one single injection of carbon dioxide (CO₂) was performed at the beginning of each experiment to monitor the dilution caused by the sampled air. While NO₂ and CO₂ were obtained from gas cylinders (1000 ppm of 99.5%; Basi Schöberl GmbH), ozone was typically in excess and generated by a silent-discharge generator (Semozon 030.2, Sorbios) as pure oxygen (99.9999%). All gases were injected into AIDA via fluorinated ethylene propylene (FEP) tubing. The duration of the gas injection ranged from a few seconds to a minute, depending on the target concentration. The concentrations of ozone, nitrogen dioxide,

Aerosol Interaction and Dynamics in the Atmosphere AIDA chamber

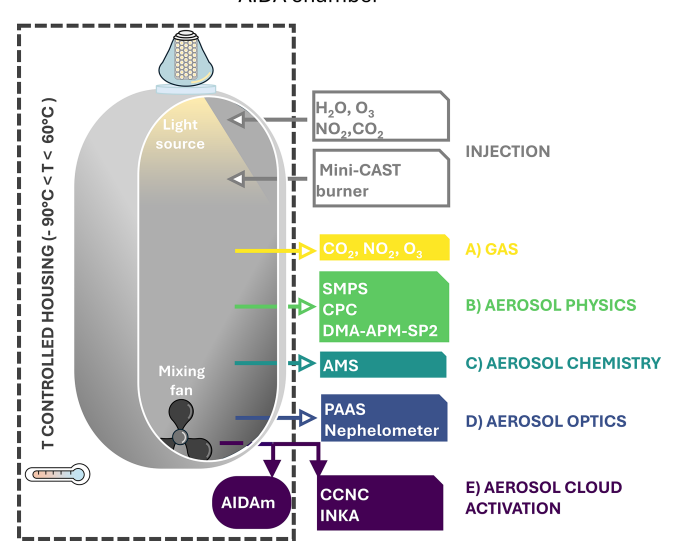


Figure 2. Schematic representing the AIDA (Aerosol and Dynamics of the Atmosphere) chamber facility. In gray are the injection systems for water vapor (H₂O), ozone (O₃), nitrogen dioxide (NO₂), carbon dioxide (CO₂), and soot (mini-CAST burner). In color, from top to bottom, are the measurements packages of (A) gas (CO₂, NO₂, O₃), (B) aerosol physics (condensation particle counter – CPC, scanning mobility particles sizer – SMPS, single-particle soot photometer – SP2, differential mobility analyzer – aerosol particle mass analyzer – DMA-APM), (C) aerosol chemistry (aerosol mass spectrometer – AMS), (D) optical aerosol properties (photoacoustic aerosol absorption photometer – PAAS, nephelometer), and (E) cloud activation (AIDA-mini – AIDA-m, cloud condensation nuclei counter – CCNC, Ice Nucleation instrument of the Karlsruhe Institute of Technology – INKA).

and carbon dioxide were measured with different gas sensors (Fig. 2). For nitrogen dioxide, the cavity phase shift NO₂ Analyzer was used (AS32M Environment S. A.); for ozone, the UV photometric ozone monitor was used (O341M Environment S. A.); and, for CO₂, the multi-gas infrared analyzer (NGA2000 MLT, Rosemount) was used. All of these gas sensors were connected to the chamber through FEP tubes. Sampling from AIDA was performed intermittently using automated valves to reduce the dilution of the AIDA air. More details on gas injection and measurement are given by Saathoff et al. (2009), Gao et al. (2022), and Vallon et al. (2022).

For the benefit of the reader, the look-up table of all particle properties and their corresponding symbols as defined in this and the following sections is given in Appendix A (Table A1).

2.4 Injection and measurement techniques of aerosol particles

2.4.1 Soot aerosol generation

Soot experiments have already been performed in the past in the AIDA chamber using various generation methods to investigate the particles' microphysics (Saathoff et al., 2003b), optical properties (Schnaiter et al., 2003, 2005), CCN activity (Henning et al., 2012), and ice nucleation activity (Möhler et al., 2005) and to calibrate-compare measuring techniques (Laborde et al., 2012b). During ARCTEx, soot particles were produced with a mini-CAST burner (series 5200; Jing Ltd Zollikofen, BE, Switzerland) operated with 60 mL min⁻¹ of propane, 1.55 L min⁻¹ of oxidation air, 7.5 L min⁻¹ of N₂, and 13 L min⁻¹ of dilution air. Due to the high internal volume of the AIDA chamber, to reach the target number concentration $(4.5 \times 10^4 \, \text{cm}^{-3})$ of soot particles, the injection time lasted between 40 and 50 min. The functioning principle of the burner and the soot properties are described in detail by Moore et al. (2014). The term "soot" is commonly used in combustion research to describe carbonaceous particles formed from incomplete combustion (Petzold et al., 2013). To maintain consistency with atmospheric science terminology, we will use "BC" to describe the evolution of particle properties, except when referencing past studies focused on combustion processes. In addition to BC particles, the mini-CAST burner emits a wide range of volatile and semi-volatile organic compounds (Mamakos et al., 2013; Mason et al., 2020; Daoudi et al., 2023). Although the burner was configured to maximize soot production while minimizing the organic content of the particles (Ess and Vasilatou, 2019), a certain number of volatile organic compounds (VOCs) were inevitably co-emitted and introduced into the AIDA chamber during injection.

2.4.2 Concentration and size distribution of total and refractory black carbon aerosol

The total number concentration of aerosol particles with a diameter above 2.5 nm was measured with a condensation particle counter (CPC, model 3776; TSI Inc, St. Paul, MN, USA). Particle size distribution was measured between 13 and 750 nm by a scanning mobility particle sizer (SMPS) utilizing a differential mobility analyzer (DMA; TSI Inc, St. Paul, MN, USA) connected to a CPC (3772, TSI Inc, St. Paul, MN, USA). Data were corrected for multiple charges and diffusion with the Aerosol Instrument Manager software.

A single-particle soot photometer (SP2, Droplet Measurement Tehcnologies, Longmont, CO, USA) was used to quantify the mass of refractory black carbon particles (rBC; Petzold et al., 2013). Previous works provide detailed descriptions of the operating principle (e.g., Stephens et al., 2003; Moteki and Kondo, 2010), calibration procedures (e.g., Gysel et al., 2011; Laborde et al., 2012a), and measuring limitations (e.g., Gysel et al., 2012; Zanatta et al., 2021; Schwarz

et al., 2022) of the SP2. The incandescent light detector was calibrated with a fullerene soot standard from Alfa Aesar (stock no. 40971, lot no. FS12S011) mass-selected with an aerosol particle mass analyzer (APM; Kanomax Model APM-3600; Ehara et al., 1996). The SP2 provided the number concentration ($N_{\rm rBC}$), the mass concentration ($M_{\rm rBC}$), and the size distribution of rBC particles in the 0.40–180 fg mass range, converted to a mass-equivalent diameter $(D_{\rm rBC})$ using a fixed bulk density. Instead of using the canonical density of ambient BC (1800 kg m⁻³; Moteki and Kondo, 2010), we used a bulk density of 1543 kg m^{-3} , which is representative of soot produced with a mini-CAST and characterized by a dominant fraction of elemental carbon over the total carbon (16%; Yon et al., 2015). The rBC mass concentration was corrected for the narrow detection range of the SP2 by calculating the missing mass between 10 and 1000 nm with a lognormal fit of the rBC mass size distribution (Pileci et al., 2021; Zanatta et al., 2018). The missing mass was attributed to the lower detection limit of the SP2 and the relatively small size of the injected particles (Fig. S1 in Sect. S1 of the Supplement). During the first 2 h after injection, the undetected mass was estimated to range between 2 % and 5 %. However, as coagulation-driven growth progressed, the rBC particles shifted fully into the SP2 detection range within approximately 6 h, effectively eliminating the initial under-detection issue. The scattering detector was calibrated using monodisperse spherical polystyrene latex (Thermo Fisher Scientific, Waltham, Massachusetts, USA). Due to suboptimal combination of the low signal-to-noise ratio of the scattering and position-sensitive detectors and the small optical size of the particles present in the AIDA chamber, it was not possible to quantify the coating thickness with SP2 measurements, as proposed by Gao et al. (2007). More details are given in Sect. 2.4.6.

Furthermore, considering, the fact that the concentration measured by the SP2 may be biased by 4% already at an aerosol number concentration of 1000 cm⁻³ (Schwarz et al., 2022), the SP2 was sampling the AIDA air after a dilution system. The dilution was modulated from a factor of 100 to a factor of 1 depending on the concentration within AIDA to maintain the rBC number concentration measured by the SP2 below 1000 cm⁻³. The dilution factor was quantified as the ratio of the number concentration measured by an undiluted reference CPC and by an auxiliary CPC connected in parallel to the SP2 behind the dilution system. All number and mass concentrations reported hereafter refer to the actual temperature and pressure conditions inside the AIDA chamber (i.e., not normalized to standard conditions) at the time of the measurement.

2.4.3 Chemical characterization of non-refractory aerosol particles

A high-resolution time-of-flight aerosol mass spectrometer (AMS) (Aerodyne Research Inc., USA) equipped with

a PM_{2.5} aerodynamic lens was used to measure the nonrefractory PM_{2.5} (NR-PM_{2.5}) components including organics, nitrate, sulfate, ammonium, and chloride at a time resolution of 1 min (DeCarlo et al., 2006; Williams et al., 2013). Chamber air was sampled via a stainless-steel tube with a total flow of 1.1 standard liter per minute, of which \sim 84 cm³ min⁻¹ was sampled by the AMS. The aerosol particles were then focused into a narrow beam by the PM2.5 aerodynamic lens with an effective transmission for particle sizes ranging from ~ 70 to ~ 2500 nm (vacuum aerodynamic diameter) and were heated by a vaporizer at 600 °C. The resulting vapors are ionized by electron impact (70 eV) and are characterized by a time-of-flight mass spectrometer. The AMS ionization efficiency was calibrated by using $\sim 400 \, \text{nm}$ dried ammonium nitrate aerosol particles. The AMS data were analyzed with the software package SQUIRREL 1.60C and PIKA 1.20C. To account for the effect of particle bouncing loss, chemical-composition-based collection efficiencies (~ 0.5) were applied to calculate the particle mass concentration (Middlebrook et al., 2012). Elemental analysis of organic aerosol, including the hydrogen-to-carbon ratio (H:C) and the oxygen-to-carbon ratio (O:C), was calculated using the improved ambient method (Canagaratna et al., 2015). In this study, the AMS was used to determine the chemical composition of non-refractory coating material deposited on the BC surface, similarly to Cross et al. (2010). Since sulfate, ammonium, and chloride were not introduced into the AIDA chamber directly or indirectly as a byproduct of combustion, their consistently remained below the detection limit. The soot produced by the mini-CAST burner contains minimal organic carbon (Moore et al., 2014), but volatile organic compounds emitted as combustion byproducts(Mamakos et al., 2013; Daoudi et al., 2023) may oxidize to form organic coatings (Lim et al., 2019). As a result, organic aerosol was observed during all experiments. In view of these considerations, the coating was assumed to consist solely of nitrate and organic components. Additionally, given that changes in particle shape and morphology during the experiments may impact the AMS collection efficiency (Willis et al., 2014), only the mass fractions of nitrate (FM_{nit}) and organics (FM_{org}) are discussed in this work.

2.4.4 Effective density and fractal dimension

The effective density (ρ_e) describes the apparent density of aspherical–fractal particles with voids, where the physical diameter does not correspond to the mobility diameter (DeCarlo et al., 2004). The fractal dimension (d_f) describes the mass–diameter relationship as a power-law function (Park et al., 2004). During ARCTEx, ρ_e and d_f were quantified by means of a DMA-APM system, similarly to Park et al. (2004). The particles were first selected with a differential mobility analyzer (DMA; TSI model 3080L; Knutson and Whitby, 1975) according to their mobility diameter ($D_{p\text{-DMA}}$). The particle mass ($m_{p\text{-APM}}$) was calculated

as the mean of the normal curve fitted to the mass distribution measured with an aerosol particle mass analyzer (APM; Kanomax Model APM-3600; Ehara et al., 1996) combined with a condensation particle counter (CPC; TSI model 3775). ρ_e was calculated as follows:

$$\rho_{\rm e} = \frac{6m_{\rm P-APM}}{\pi D_{\rm P-DM\Delta}^3}.\tag{1}$$

 $\rho_{\rm e}$ measurements were performed before and after the daily change of conditions within AIDA in the mobility diameter range of 100–500 nm, with a diameter resolution of 50 nm. Due to varying rates of particle concentration and diameter across experiments, $\rho_{\rm e}$ calculations were consistently available only in the 150–250 nm mobility diameter range. The uncertainty of $\rho_{\rm e}$ was quantified as the standard deviation of a normal curve fitted to the mass distribution measured by the APM during all scans performed between 150–250 nm (9 %).

Following Park et al. (2004), the relationship between particle mass and its diameter is described as a power law, where the exponent represents the fractal dimension (d_f) , and k_f is a fit constant.

$$m_{\text{P-APM}} = k_{\text{f}} D_{\text{P-DMA}}^{d_{\text{f}}} \tag{2}$$

The $d_{\rm f}$ error associated with each scan was calculated as the standard deviation of the fit function assuming a 95 % confidence interval. Overall, the averaged $d_{\rm f}$ error was quantified to be 13 %, with increasing values at the end of each experiment, when particle number concentration was lower. Considering the various measuring approaches (Cross et al., 2010), the so-defined $d_{\rm f}$ is alternatively called the "fractal exponent" (Kim et al., 2009) or "scaling exponent" (Sorensen, 2011), which is analogous although not strictly equivalent to fractal dimension, remaining mostly qualitative (Yon et al., 2015).

2.4.5 Mixing state and particle density

The SP2 can be combined with independent aerosol mass quantification techniques to determine aerosol mixing states in both field and laboratory experiments (Sipkens et al., 2021; Naseri et al., 2022). During ARCTEx, the SP2 was used downstream of the DMA-APM system, which was operated in size—mass selection mode. This setup allowed for quantification of the refractory black carbon mass ($m_{\rm rBC-SP2}$) within the total particle mass selected by the APM ($m_{\rm p-APM}$). The rBC mass ($m_{\rm rBC-SP2}$) was calculated by fitting a normal curve to the mass distribution of rBC particles measured by the SP2 after the DMA-APM selection. The mass fraction of rBC (Fm_{rBC}) was determined as the ratio of $m_{\rm rBC-SP2}$ to $m_{\rm p-APM}$. Using this, the coating mass fraction (Fm_{coat}) was calculated as follows:

$$Fm_{coat} = \frac{m_{P-APM} - m_{rBC-SP2}}{m_{P-APM}}.$$
 (3)

The uncertainty of Fm_{coat} was quantified as the standard deviation of a normal curve fitted to the mass distribution measured by the SP2 during all scans performed between 150–250 nm (15 %).

The average particle density (ρ_p) represents the density of the aerosol material. In a double-component system (rBC core and coating), ρ_p was calculated as the mass weighted mean of the density of rBC material and the coating material:

$$\rho_{\rm p} = \rho_{\rm rBC} F m_{\rm rBC} + \rho_{\rm coat} F m_{\rm coat}. \tag{4}$$

The rBC material density (ρ_{rBC}) was assumed to be 1543 kg m⁻³, which is representative of soot produced with a mini-CAST (Yon et al., 2015). Similarly, the contribution of the coating was estimated using a coating-material density (ρ_{coat}) and its mass fraction. ρ_{coat} was estimated using the AMS-derived relative mass fractions of organic (FM_{org}) and nitrate (FM_{nit}) material. ρ_{coat} was calculated as a function of the relative abundance of organics and nitrate and their corresponding material density, as in Eq. (5):

$$\rho_{\text{coat}} = \rho_{\text{org}} F M_{\text{org}} + \rho_{\text{nit}} F M_{\text{nit}}, \tag{5}$$

where $\rho_{\rm org}$ represents the organic-material density ($\rho_{\rm org}=1200~{\rm kg~m^{-3}}$; Lim and Turpin, 2002), and $\rho_{\rm nit}$ represents the nitrate-material density ($\rho_{\rm nit}=1750~{\rm kg~m^{-3}}$; Pokorná et al., 2022).

We note that this approach assumes a simplified dual-component system with a solid and void-free core shell structure and does not capture the morphology change induced by coating formation. Hence, the calculated ρ_p should be interpreted as an average material density. The ratio of ρ_p/ρ_e was used as an indicator of particle compaction. Values near unity suggest a compact particle with an internally mixed structure and minimal voids, while lower values indicate a fractal morphology, where internal voids reduce the effective density relative to the material density.

2.4.6 Volume-equivalent diameter and coating thickness

The volume-equivalent diameter ($D_{\text{ve-p}}$) is the diameter of a spherical and compact particle with the same volume (De-Carlo et al., 2004), and it is calculated from the particle mass knowing the material density (ρ_p ; Eq. 4) of the total particle as follows:

$$D_{\text{ve-P}} = \sqrt[3]{\frac{6m_{\text{P-APM}}}{\pi \rho_{\text{p}}}}.$$
 (6)

The volume-equivalent diameter of the rBC core was calculated following Eq. (7) based on the mass of the rBC-core measured with the SP2 ($m_{\rm rBC-SP2}$) behind the DMA-APM tandem using a fixed material density of 1543 kg m⁻³ (Yon et al., 2015):

$$D_{\text{ve-rBC}} = \sqrt[3]{\frac{6m_{\text{rBC-SP2}}}{\pi \rho_{\text{rBC}}}}.$$
 (7)

For each particle selected by the DMA-APM-SP2 system, based on its mobility diameter and mass, it was possible to estimate the volume-equivalent coating thickness ($\Delta D_{\rm ve}$; Eq. 8). Assuming the particle core is spherical and covered by a spherical, concentric coating layer, $\Delta D_{\rm ve}$ was defined as half of the difference between the total particle diameter $D_{\rm ve-p}$ and the rBC core diameter $D_{\rm ve-rBC}$:

$$\Delta D_{\text{ve}} = \frac{D_{\text{ve-P}} - D_{\text{ve-rBC}}}{2}.$$
 (8)

It must be noted that the SP2 is also capable of estimating the coating thickness of rBC-containing particles (Laborde et al., 2012b) by applying the leading-edge-only fit (LEO-fit) as proposed by Gao et al. (2007). To apply the method with this specific SP2 model, it is essential to obtain signals from the scattering and position-sensitive detectors with a high signalto-noise ratio for particles with an rBC core diameter in the 200-260 nm range (Zanatta et al., 2018). On one side, the number fraction of rBC cores exceeding 200 nm in diameter remained below 1 % throughout our experiments, limiting counting statistics. More importantly, even if internal mixing led to increased mobility diameters during the SL and WL experiments, the optical diameters of the rBC-containing particles remained below or close to the detection threshold of the SP2's scattering and position-sensitive detectors. Hence, although the approach proposed here involved the use of several instruments, it represented the only technical solution to determine the coating thickness for small and thinly coated BC-containing particles.

2.4.7 Climate-relevant aerosol particle properties

Climate-relevant properties of BC were quantified during ARCTEx with an extended set of instruments (Fig. 2). Optical properties such as aerosol absorption and scattering coefficient were quantified at various wavelengths with a photoacoustic aerosol absorption spectrometer (KIT-PAAS; Linke et al., 2016) and a nephelometer (model 3563, TSI Inc, St. Paul, MN, USA; Anderson and Ogren, 1998), respectively. The ability of BC to activate to cloud droplets was quantified with a cloud condensation nuclei counter (CCNC; Droplet Measurement Technologies – DMT, Longmont, CO, USA; Rose et al., 2008). The ice-nucleating behavior was quantified at constant temperature and varying supersaturation with the Ice Nucleation Instrument of the Karlsruhe Institute of technology (INKA; Bertozzi et al., 2021) and under the same thermodynamic conditions as in AIDA with the AIDA-mini (AIDAm; Vogel et al., 2022). While the present work aims to present the ARCTEx project and to assess the evolution of fundamental BC properties, the evolution of climate-relevant properties as a function of aging will be the topic of study for a companion paper.

2.5 Experimental design

In light of the complexity of ARCTEx simulations, we provide a description of the experimental design and schedule. The experiments relied on the assumption that 1 d of experiments corresponded to 10° of northward transport; hence, the full transport conditions from 40 to 90° N were reproduced during 5 d of experiments. The temporal evolution of each experiment was represented with the elapsed time, in hours, since the beginning of aging (t_0) , corresponding to a simulated latitude of 40° N. Thus, t_{24} corresponded to 50° N, t₄₈ corresponded to 60° N, t₇₂ corresponded to 70° N, t₉₆ corresponded to 80° N and t_{120} corresponded to 90° N. The simulation of northward transport and the aging process started at the first virtual sunrise (t_0) with the first injection of trace gas and light irradiation. Every 24 h and 10° N, the chamber conditions such as temperature, humidity, light (irradiation time), and concentration of NO2 and O3 were adjusted to match the transport conditions identified from the reanalysis data. Gas concentrations were continuously monitored using the instruments described in Sect. 2.3, while aerosol physical and chemical properties were measured as outlined in Sect. 2.4. The experiment preparation occurred before t_0 (negative elapsed time) and included the cleaning and cooling of the chamber (t_{-24}) , the single injection of BC (t_{-2}) , its characterization under dark conditions (t_{-1}) , and the single injection of $CO_2(t_{-1})$.

A detailed and idealized schedule for the experimental sequence of operations is given in Table 1.

3 Results

This section presents the experimental results in a structured progression. We begin with three preparatory analyses: first, the transport conditions simulated in AIDA (Sect. 3.1), followed by a characterization of the initial BC particle properties (Sect. 3.2) and then an evaluation of the temporal evolution of particle number and mass concentrations in comparison to real Arctic conditions (Sect. 3.3). The core of the results focuses on the chemical, morphological, and size evolution of BC during aging (Sect. 3.4). Finally, we assess the aging timescales of BC under different transport scenarios (Sect. 3.5).

3.1 Northward-transport conditions

We start our discussion with the latitudinal profiles of the atmospheric conditions, extracted from ERA-5 and the CAMS reanalysis, for the four transport scenarios of summer, low altitude (SL); summer, high altitude (SH); winter, low altitude (WL); and winter, high altitude (WH). Figure 3 shows the latitudinal profiles of temperature, relative humidity, and NO₂ / BC ratio. The temperature decreased with latitude in all experiments, with the strongest gradient at low altitudes in summer (0 °C < T < 21 °C) and win-

ter $(-21 \,^{\circ}\text{C} < T < -9 \,^{\circ}\text{C})$. A weaker gradient but marked low temperatures were observed at high altitudes in summer $(-41 \,{}^{\circ}\text{C} < T < -35 \,{}^{\circ}\text{C})$ and winter $(-58 \,{}^{\circ}\text{C} < T < -52 \,{}^{\circ}\text{C})$. Relative humidity increased with latitude up to 80 % in the low-altitude scenarios, while more stable and drier conditions were observed at high altitudes (RH < 65 %). These temperature and humidity profiles are consistent with general Arctic conditions, which typically feature stronger latitudinal cooling and more humid conditions near the surface compared to at higher altitudes (Przybylak, 2016). The longer atmospheric lifetime of NO₂ during winter (Levy et al., 1999) may be responsible for the higher NO₂ / BC ratio in winter than in summer in both low- and high-altitude scenarios. Although elevated NO₂ relative to BC concentration is a prerequisite for nitrate coating formation, the production pathways in the Arctic are strongly influenced by extreme environmental factors such as low temperatures (Alexander et al.; 2020) and limited sunlight (Schaap et al., 2004), which affect both the efficiency and timing of nitrate formation. As concluded in the recent AMAP (2021) report, the limited horizontal and vertical coverage of NO₂ measurements does not allow for further comparison with ambient data.

To verify the representativity of the AIDA simulations, we compared the reanalysis "set points" with the daily mean values observed in the chamber (Fig. 3). For all of the considered scenarios, we were able to reproduce the latitudinal profile of temperature with a relative precision of 1 %, without introducing any bias. The difference between the simulated and measured RH showed higher variability than temperature. This difference was not systematic and varied from a maximum overestimation of +27% (day 1 of WH) to -20%(day 1 of SL). Despite this, we were able to reproduce in the AIDA chamber the latitudinal RH gradient extracted form ERA-5. The mismatch in RH may have affected gas-phase and aqueous-phase chemistry processes influencing the formation of coating precursors and coating material. As shown by the high values of the standard deviation of the NO₂ / BC ratio measured in the AIDA chamber, the control of NO₂ concentration proved to be the most complicated. This technical difficulty led to non-systematic bias during the various experiments. As an example, we introduced contrasting bias in the low-altitude scenarios. While the high NO₂ / BC in SL might promote a higher degree of internal mixing in AIDA compared to in CAMS, the depleted level of NO₂ might have hindered coating formation and internal mixing in WL. In summary, atmospheric conditions extracted from ERA-5 and CAMS revealed complex and heterogeneous transport conditions, which were well reproduced, day-by-day, in the AIDA chamber. Nonetheless, discrepancies between reanalysis and measured NO₂ levels might accelerate or hinder coating formation in a non-systematic way across the experiments. The means of these atmospheric conditions extracted from the reanalysis and AIDA dataset are listed in Sect. S2 of the Supplement (Tables S1 and S2).

Table 1. Schedule for the experimental sequences.

Elapsed time [h]	Experiment day	Simulated latitude [° N]	Operation	
-24	-1	_	Chamber cleaning and conditioning	
-3	1	_	Background measurement	
-2	1	_	Soot injection	
-1	1	_	Dark characterization	
0	1	40–50	O ₃ and NO ₂ injection Light on	
+22	1	40–50	Temperature adjustment	
+24	2	50–60	O ₃ –NO ₂ injection Water vapor injection ^a Light adjustment ^b	
+46	2	50-60	Temperature adjustment	
+48	3	70–80	O ₃ –NO ₂ injection Water vapor injection ^a Light adjustment ^b	
+70	3	70–80	Temperature adjustment	
+72	4	80–70	O ₃ –NO ₂ injection Water vapor injection ^a Light adjustment ^b	
+94	4	80–90	Temperature adjustment	
+96	5	80–90	O ₃ –NO ₂ injection Water vapor injection ^a Light adjustment ^b	
+110-120	5	80–90	End of experiment	

^a Since the sampling air was replaced by dry air, the water vapor was replenished every day. ^b The solar simulator was adjusted to illuminate the chamber with radiation representative of the corresponding latitude.

3.2 Characterization of fresh mini-CAST soot

The physical characterization of fresh soot produced with the mini-CAST was performed before t_0 (Table 1) and is fully described in Sect. S3 of the Supplement. The key findings are summarized as follows. The SMPS-measured geometric mean diameter ranged from 80 nm (SL) to 104 nm (SH) (Fig. S2a), consistently with prior studies using diffusion flame burners with similar oxidative airflows (Ess et al., 2021; Maricq, 2014; Moore et al., 2014; Rissler et al., 2013). Figure S2b shows that the diameter-dependent decrease in effective density is comparable to precedent studies with diffusion flame soot (Cross et al., 2010; Rissler et al., 2013; Ess et al., 2021). The low fractal dimensions ($d_f = 2.01-2.21$) of the generated particles (Fig. S2c) matched those reported previously for diffusion flame soot (Ess et al., 2021; Rissler et al., 2013; Heuser et al., 2025), diesel soot (Olfert et al., 2007), and premix flame soot (Cross et al., 2010). The rBC mass fraction ($F_{\rm rBC}$) varied between 95 % and 75 %, in agreement with ratios of elemental to total carbon from premixed (Cross et al., 2010) and diffusion (Schnaiter et al., 2006; Ess et al., 2021; Heuser et al., 2025) burners. Note that rBC and elemental carbon should be compared cautiously (Pileci et al., 2021). The soot produced during ARCTEx featured complex geometry and a dominant refractory mass fraction. While our soot properties fell within the range reported in previous studies, the unique experimental design and setup of ARCTEx may account for the differences observed compared to earlier experiments.

3.3 Evolution of particle number and mass concentrations

In this section, we briefly discuss the variability in number and mass concentrations as measured with the SP2. A target concentration of 4.5×10^4 cm⁻³ at t_{-1} was chosen to ensure the suspension of at least a few hundred particles per cm³ after 120 h. This accounted for a dilution factor of

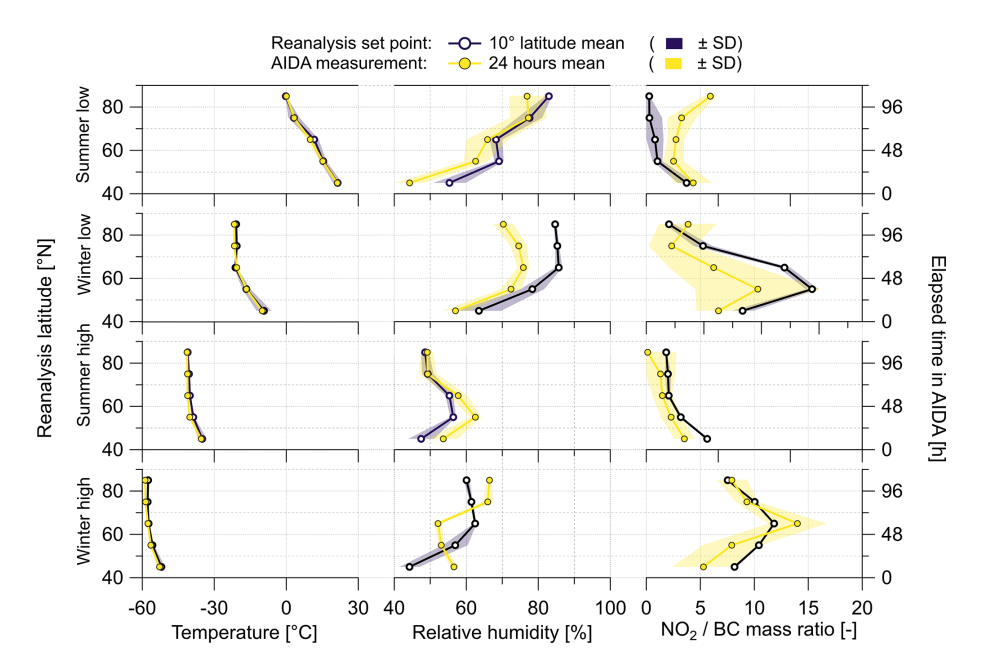


Figure 3. Left axis: latitudinal profiles of temperature and relative humidity extracted from ERA-5 and of NO_2 / BC mass ratio extracted from CAMS in the region of interest (40–90 $^{\circ}$ N and 60–140 $^{\circ}$ E). Mean and standard deviation (SD) calculated for equidistant latitude bands 10° wide. Right axis: temporal variability of temperature, relative humidity, and NO_2 / BC ratio as measured in the AIDA chamber. Mean and standard deviation (SD) calculated over 24 h.

25 %-30 % per day, which was driven by the sampling flow of the gas and aerosol measuring instruments. Overall, $N_{\rm rBC}$ remained above $300 \,\mathrm{cm}^{-3}$ until 110–115 h after t_0 , enough time to perform a full characterization of its chemical and physical properties. In terms of mass concentration, the rBC levels decreased during all scenarios from a maximum of $15 \,\mu \text{g m}^{-3}$ at t_0 to a minimum of $0.5 \,\mu \text{g m}^{-3}$ at t_{115} (Fig. 4). Although the concentrations in AIDA were adjusted to ensure the extended duration of the experiments and to approximate near-real conditions (based on the NO₂ / rBC mass ratio), it is insightful to compare these values with previous rBC mass concentrations measured by SP2 in various environments. Due to the utilization of similar rBC concentrations in low- and high-altitude scenarios for experimental reasons, it is evident that the ARCTEx concentrations do not accurately reflect the natural decreasing trend of rBC with altitude as observed across Europe (McMeeking et al., 2010; Dahlkötter et al., 2014; Zanatta et al., 2020) and in the high and low Arctic (Schulz et al., 2019; Jurányi et al., 2023; Zanatta et al., 2023). The $M_{\rm rBC}$ observed during the first 24 h (40-50° N) was representative of polluted Asian megacities ($\sim 20 \,\mu \text{g m}^{-3}$; Li et al., 2023; Yu et al., 2020). M_{rBC} on the second day (50-60° N) reflected pollution events over continental Europe ($\sim 4 \,\mu g \, m^{-3}$; Laborde et al., 2013; Yuan et al., 2020). Although decreasing due to particle dilution, $M_{\rm rBC}$ remained above the typical Arctic background values of northern Finland (0.12 µg m⁻³; Raatikainen et al., 2015) and values of European Arctic haze (0.04 µg m⁻³; Zanatta et al., 2018).

3.4 Evolution of BC morphology and mixing state during aging

In this section, we describe the temporal evolution of the morphology and mixing composition of particles in the 150–250 nm diameter range as described in Sect. 2.4.4 and 2.4.5. These properties include the particle effective density (ρ_e ; Fig. 5a), the particle fractal dimension (d_f ; Fig. 5b), the mass fraction of coating material (Fm_{coat}; Fig. 5c), the total particle density (ρ_e / ρ_p ; Fig. 5d), the ratio of effective to particle density (ρ_e / ρ_p ; Fig. 5e), and the volume-equivalent coating thickness (ΔD_{ve} ; Fig. 5f). The mass fraction of nitrate (FM_{nit}) and organics (FM_{org}) is shown in Fig. 6. Excluding FM_{nit} and FM_{org}, the other properties described in this section were calculated from the DMA-APM and DMA-APM-SP2 scans. These scans were performed before and after the virtual midnight, resulting in a low temporal resolution.

3.4.1 Organic-driven aging of BC in summer low-altitude transport

During the SL experiment, ρ_e , d_f , and Fm_{coat} increased significantly from t_0 (40° N) to t_{96} (80° N), indicating a profound change in the morphology and mixing of BC (Fig. 5a-c). Although ρ_e increased by a factor of 2 and Fm_{coat} reached 50% in the first 24 h (40–50° N) already, clear indications of particle compaction were only observed after t_{48} , when d_f increased to values of between 2.5 and 2.8 (60–70° N). At this stage, ρ_e varied within 614–982 kg m⁻³, and Fm_{coat} varied within 56%–63%. Organics dominated the overall composi-

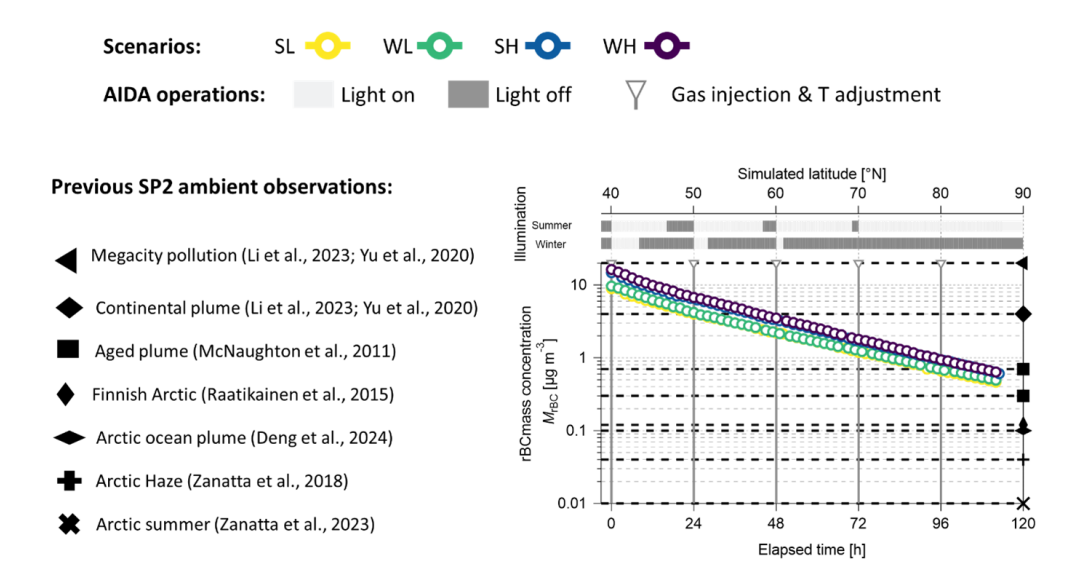


Figure 4. Temporal and latitudinal evolution of rBC mass concentration measured with the single-particle soot photometer SP2 between 0.40–180 fg. Concentrations are normalized to the gas temperature and pressure of the AIDA chamber at the time of measurement. ARCTEx scenarios: summer, low altitude (SL); winter, low altitude (WL); summer, high altitude (SH); winter, high altitude (WH). Concentration compared with previous ambient $M_{\rm rBC}$ observations.

tion of coatings, with FM_{org} constantly above 90 % (Fig. 6a). Considering the fact that O_3 decreased at a faster rate compared to the other scenarios, the long irradiation time might promote the photolysis of ozone to form OH radicals. In turn, OH may oxidize volatile organic carbon, emitted by the burner (Mamakos et al., 2013; Daoudi et al., 2023), to secondary organic material (Lim et al., 2019). This reaction pathway efficiently competed with the oxidation of NO_2 to nitric acid and its condensation to nitrate coating during the daytime (Alexander et al., 2009). The low NO_2 /BC ratio and prolonged irradiation time prevented the typical nitrate night-formation pathways via NO_3 reaction with volatile organic carbon (Ng et al., 2017) or with NO_2 to form N_2O_5 , followed by hydrolysis on the BC surface (Chang et al., 2011; Alexander et al., 2020).

Given that organic material has a lower density than nitrate and BC, the nearly constant FM_{org} combined with an increase in Fm_{coat} resulted in a steady decrease in particle density, contrasting with the increase observed in the other experiments (Fig. 5d). Nonetheless, ρ_e (1350 kg m⁻³) approached ρ_p (1299 kg m⁻³) at the end of the experiment at t_{96} (Fig. 5e). Since the effective density and material density are equivalent for spherical particles, a 4% difference suggests that BC particles in SL attained sphericity. It must be noted that uncertainties in the AMS measurements (Liu et al., 2007) or assumptions regarding the highly variable organic density (Kostenidou et al., 2007) might influence this result. In light of this and considering the coating composition and the overarching assumption of sphericity, the volume-equivalent coating thickness (Fig. 5f) monotonically

increased from $\sim 10 \text{ nm}$ at t_{24} (40–50° N) to 41 nm at t_{96} (80° N).

3.4.2 Nitrate-driven aging of BC in winter low-altitude transport

During the WL experiment, ρ_e increased rapidly from $\sim 200 \,\mathrm{kg} \,\mathrm{m}^{-3}$ to approximately $1500 \,\mathrm{kg} \,\mathrm{m}^{-3}$ within $48 \,\mathrm{h}$ of aging (60° N), after which it remained constant until t₉₆ (80° N), indicating the formation of spherical particles (Fig. 5a). This compaction towards sphericity was confirmed by $d_{\rm f}$ values approaching 3 after 48 h, although some unphysical values above 3 were observed due to limited DMA-APM scans (Fig. 5b). These values might reflect the $\pm 13\%$ error associated with the fitting method used to derive $d_{\rm f}$ (Sect. 2.4.4). The increase in Fm coat from 23 % to 87 % within the first 48 h, peaking at 97 % by t_{96} , suggests that winter low-altitude conditions can lead to fully encapsulated BC particles within 2 d or before reaching 60° N (Fig. 5c). In contrast to the SL scenario, the higher NO₂ / BC ratio favored nitrate formation over organic coatings, with a rapid increase in the nitrate mass fraction (FM_{NO₃}) during irradiation periods (Fig. 6b). This increase suggests that nitrate formed via OH radical oxidation to nitric acid, which then condensed onto the BC, with limited competition from secondary organic aerosol formation, as in the case of SL. The complete darkness during the last 3 experimental days likely promoted nighttime nitrate formation while preventing photolysis of gas precursors (NO₃; Dorn et al., 2013) and nitrate (Ye et al., 2017). As a result, FM_{NO3} increased sharply in the first 7 h to 60 %, reaching 88 % after 48 h (60° N) and 93 % after 114 h ($\sim 90^{\circ}$ N). In opposition to summer, the increas-

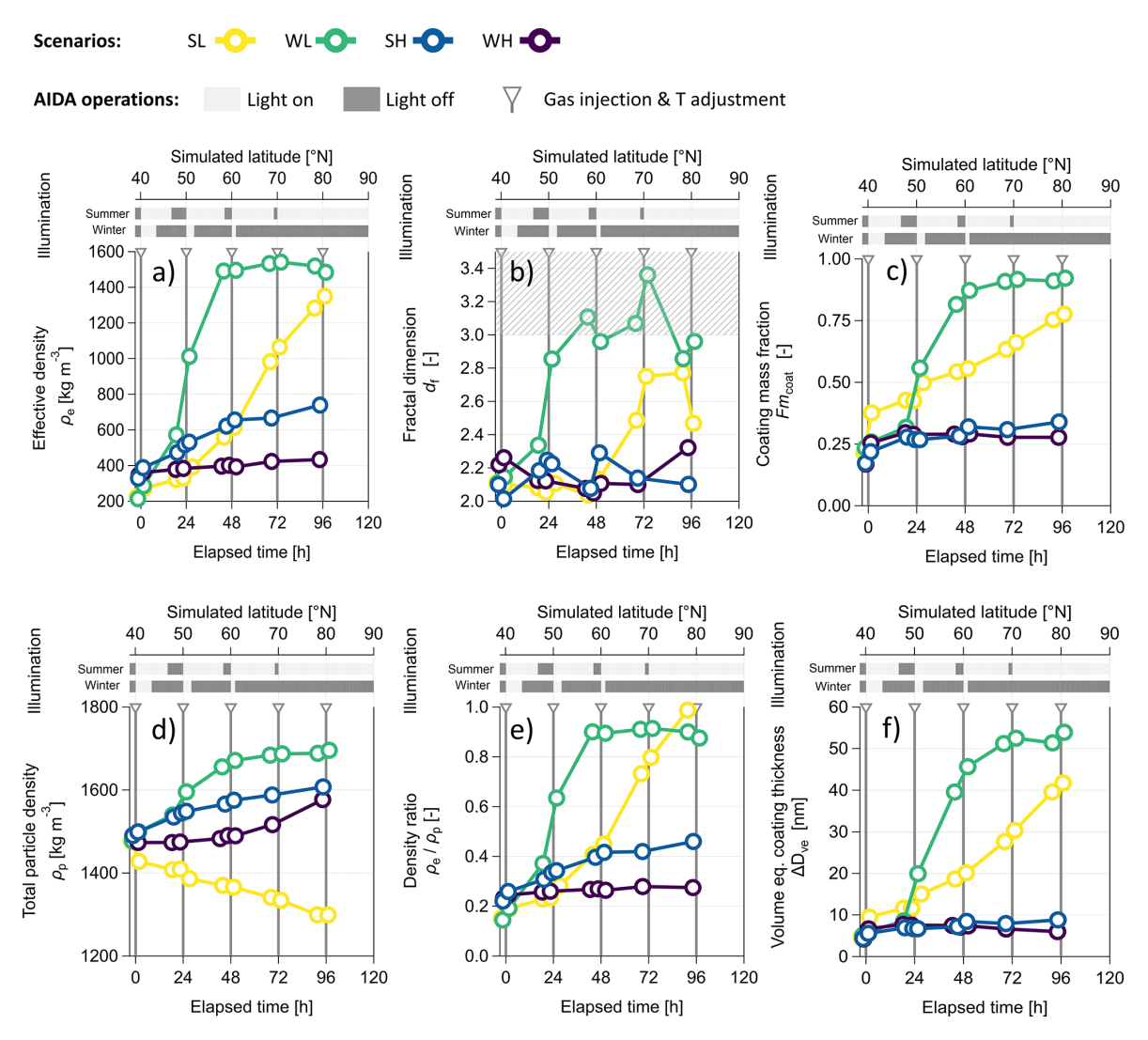


Figure 5. Temporal and latitudinal evolution of rBC physical properties. (a) Particle effective density, ρ_e ; (b) particle fractal dimension, d_f ; (c) coating mass fraction, Fm_{coat}; (d) total particle density, ρ_p ; (e) ratio of effective to particle density, ρ_e/ρ_p ; (f) volume-equivalent coating thickness, ΔD_{ve} . All properties were calculated for particles with a mobility diameter of between 150–250 nm. ARCTEx scenarios: summer, low altitude (SL); winter, low altitude (WL); summer, high altitude (SH); winter, high altitude (WH).

ing dominance of nitrate led to an increase in particle density to $\sim 1700 \, \mathrm{kg} \, \mathrm{m}^{-3}$ (Fig. 5d), agreeing within 10 % with the final effective density (Fig. 5e). This supports the hypothesis of BC already becoming fully encapsulated by a coating after 48 h of aging. Assuming a concentric core shell structure, the coating thickness was initially thin (< 10 nm) in the first 24 h (50° N) but increased to 45 nm at t_{48} (60° N) and ultimately reached the highest value of all ARCTEx scenarios, with 54 nm, at t_{96} (80° N; Fig. 5f).

3.4.3 Slower aging during high-altitude transport

Despite the different chemistry and timescales, both SL and WL scenarios led to significant BC aging, producing fully encapsulated, spherical particles. In contrast, particle mor-

phology and mixing showed a weaker evolution during highaltitude transport in both summer and winter. The effective aerosol particle density ρ_e increased by a factor of 2.24 during SH and by a factor of 1.25 during WH from t_0 to t_{96} , a substantially smaller change compared to in the low-altitude experiments (Fig. 5a). Although some compaction was observed, especially in SH, d_f and Fm_{coat} never exceeded 2.4 and 35%, respectively, in both scenarios (Fig. 5b and c). This indicates a very small degree of aging, with limited impacts on the morphology of the BC particles at very low temperatures from mid-latitudes to the Arctic. Under these conditions of persistent asphericity and negligible mixing, the coating chemistry and thickness quantification are highly uncertain. However, nitrate dominated the composition of coating (Fig. 6c and d), ρ_e/ρ_p remained well below unity

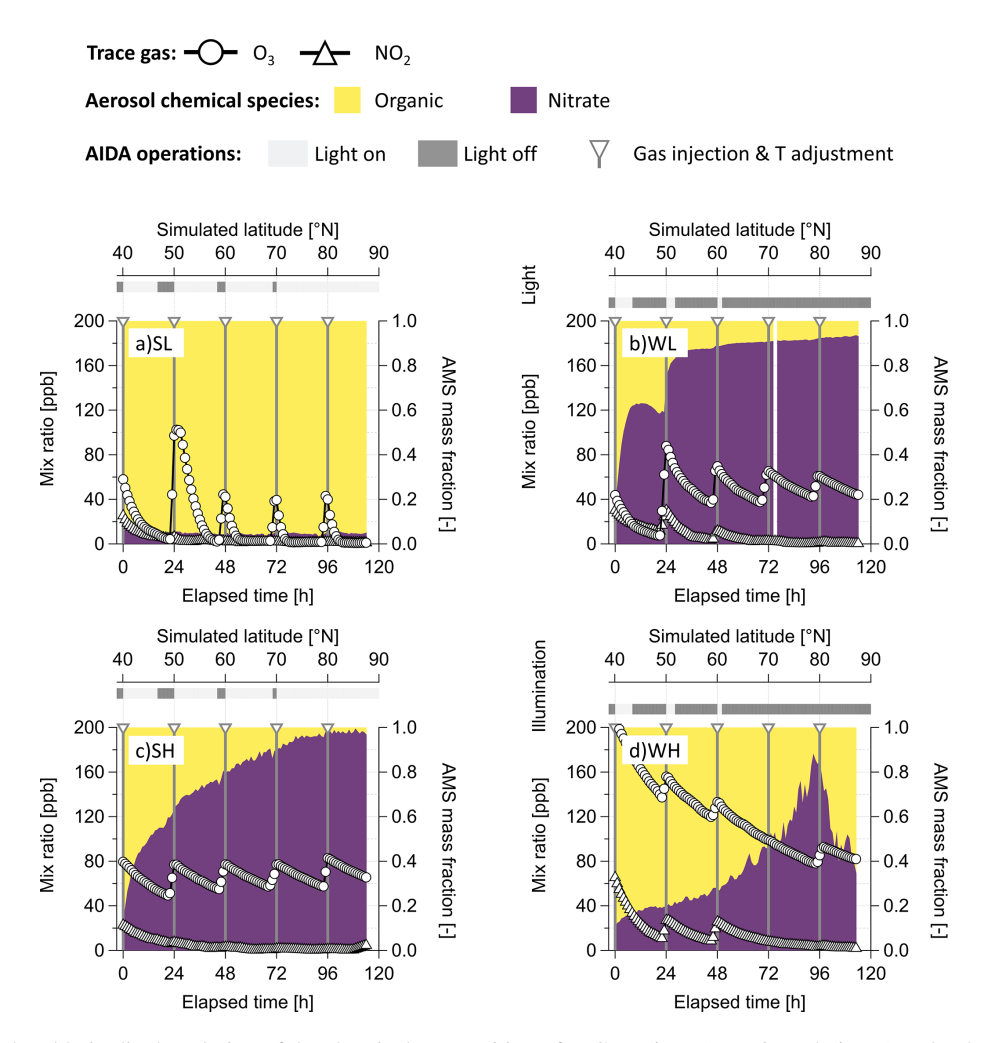


Figure 6. Temporal and latitudinal evolution of the chemical composition of rBC coatings (organic and nitrate) and volume mixing ratio of ozone (O_3 in circles) and nitrogen dioxide (NO_2 in triangles) during the ARCTEx scenarios: (a) summer, low altitude (SL); (b) winter, low altitude (WL); (c) summer, high altitude (SH); (d) winter, high altitude (WH).

(Fig. 5e), and $\Delta D_{\rm ve}$ remained below 10 nm until t_{96} or 80° N (Fig. 5f). Hence, high-altitude transport may slow the aging process of BC, resulting in completely different BC properties in the Arctic region as a function of altitude. This aging reduction was likely linked to low temperatures, which may reduce the yield of ozone photolysis slightly (Matsumi et al., 2002), shorten the lifetime of HNO₃ (Dulitz et al., 2018), and minimize the oxidation of volatile organic compounds to secondary organic aerosol coatings (Saathoff et al., 2009; Tillmann et al., 2009). This hypothesis is reinforced by the near-constant depletion rates of NO2 and O3, irrespective of light conditions, suggesting limited photochemical and nocturnal reactivity at temperatures below -30 °C. Although the formation of secondary organo-nitrate aerosol is found to be temperature dependent (Gao et al., 2022), due to the lack of comprehensive gas-phase (nitric acid, OH radical, volatile organic compounds) and particle-phase (absolute quantification of nitrate, organic, and organo-nitrate compounds) chemical speciation, we cannot quantify the coating yields or attribute them to specific reaction pathways.

3.4.4 Mass closure of total aerosol

The rBC mass concentration measured by the SP2 was converted into total aerosol mass concentration ($M_{\text{p-SP2}}$) using the particle-by-particle coating mass fraction. Similarly, the number size distribution from the SMPS was converted into a mass size distribution by considering the size-dependent effective density to calculate the corresponding mass concentration ($M_{\text{p-SMPS}}$). A detailed description of the methodology is available in Sect. S4 of the Supplement. By comparing these two variables, we aim to assess the accuracy of the Fm_{coat} and ρ_e measurements.

A strong correlation between the two mass concentrations was observed across all scenarios (Fig. S3), with the lowest value in WL ($R^2 = 0.84$) and the highest in SL ($R^2 = 0.99$). However, significant variability was observed

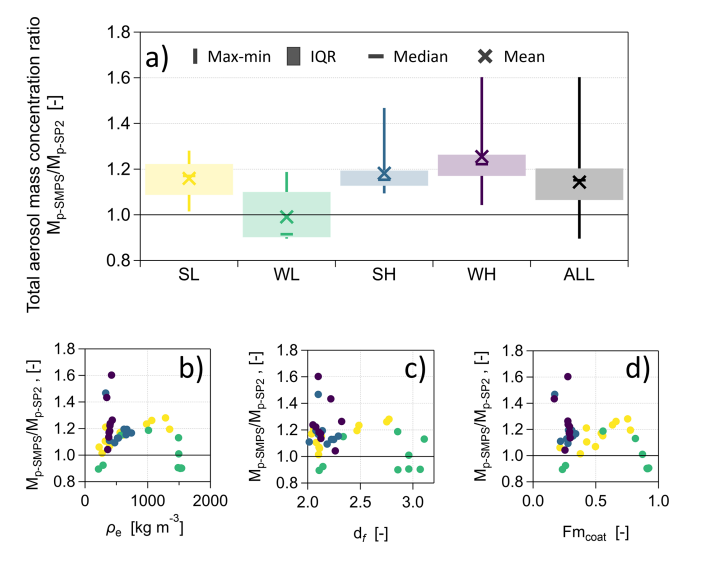


Figure 7. Comparison between the total aerosol mass concentration derived from the SMPS $(M_{\text{p-SMPS}})$ and SP2 $(M_{\text{p-SP2}})$. (a) Statistic of the $M_{\text{p-SMPS}}/M_{\text{p-SP2}}$ ratio for each scenario. Correlation of $M_{\text{p-SMPS}}/M_{\text{p-SP2}}$ ratio with (b) effective density, ρ_{e} ; (c) fractal dimension, d_{f} ; and (d) coating mass fraction, Fm_{coat}. All properties are calculated for particles with mobility diameters of between 150–250 nm.

across scenarios: the $M_{\text{p-SMPS}}/M_{\text{p-SP2}}$ ratio ranged from a maximum of 1.6 (WH) to a minimum of 0.89 (WL), with an ARCTEx average of 1.14 (Fig. 7a). This average indicates an overall overestimation of $M_{\text{p-SMPS}}$ (or $M_{\text{p-SP2}}$ underestimation), ranging from 0% in WL to 25% in WH. The $M_{\text{p-SMPS}}/M_{\text{p-SP2}}$ ratio was compared with effective density (Fig. 7b), fractal dimension (Fig. 7c), and coating mass fraction (Fig. 7d), but no clear correlations were found. Notably, the absence of coating in WH ($\rho_{\rm e} < 500\,{\rm kg\,m^{-3}}$; $d_{\rm f} < 2.4$; Fm_{coat} < 0.3) was linked to the highest discrepancies between the two methods. In contrast, little variability was seen in WL when particles were dense, spherical, and thickly coated ($\rho_{\rm e} > 1000\,{\rm kg\,m^{-3}}$; $d_{\rm f} > 2.8$; Fm_{coat} > 0.7).

Considering the instrumental uncertainties of the SMPS and the SP2, as well as the quantification uncertainties of $m_{\text{p-APM}}~(\pm 9~\%)$ and $m_{\text{rBC-SP2}}~(\pm 15~\%)$, the two mass concentrations align well within the instrumental uncertainties, confirming the reliability of the results presented in this work.

3.4.5 Aging impact on particle diameter

During all experiments, particle diameter evolved with time following different timescales (Fig. S4). The measurements of the rBC core diameter (SP2) and total particle diameter (SMPS) were used to assess intra-coagulation and coating formation, respectively. While, here, we provide a short summary, all details are given in Sect. S5 of the Supplement. Excluding WL, the rBC core diameter increased exponentially (a decreasing growth rate with decreasing concentration),

leading to a net diameter growth of between 65 % and 85 % by the experiment's end (90° N). In WL, diameter growth shifted from exponential to linear at the coating onset. The concurrent increase in fractal dimension may have reduced active surface area, limiting collisions and slowing coagulation. Despite prior studies (e.g., Schnaiter et al., 2003; Maricg, 2007), coagulation during the transition from external to internal mixing remains poorly characterized. While coagulation increases diameter while maintaining external mixing (Naumann, 2003), coating deposition first compacts and reduces the size of BC (Schnaiter et al., 2003; Bambha et al., 2013; Yuan et al., 2020) and then increases the diameter with coating thickening (Li et al., 2017). These processes were clearly visible in the low-altitude scenarios. The gradual formation of thin coating was associated with a gradual collapse of BC's ramified structure during SL and allowed us to observe a slow but steady reduction in mobility diameter. The rapid attainment of sphericity in WL did not allow us to observe compaction but, rather, the quick formation of thick coatings in every coating stage already. A similar step-wise growth was observed during medium-duration aging experiments in AIDA (Schnaiter et al., 2005).

3.5 Varying aging timescales as a function of transport pathway

Generally, the aging timescale defines the suspension time required for a BC particle to transition from a hydrophobic state to a hydrophilic state. Global models parameterize this conversion in several ways. The most simplified approach in bulk aerosol models is to consider a fixed aging timescale (Koch et al., 2009). Other aging schemes, used in modal aerosol modules, include a coating-thickness threshold made up of a variable number of mono-layers (Liu et al., 2016). Considering the large discrepancies between observations and simulations, a more detailed treatment of size, morphology, and mixing is implemented in the modules of global models (e.g., Matsui, 2016; Chen et al., 2024; Jin et al., 2025). In this section, we aim to determine the aging timescale and latitude scale of BC as a function of its degree of internal mixing rather than hygroscopicity, quantified as the ratio of coating material to the rBC core in mass (Rm_{coat}). Sedlacek et al. (2022) showed that the increase in Rm_{coat} is proportional to the age of pollution plumes, following a first-order growth model reaching a maximum of 20 within 1 d of suspension time. We first address the evolution of Rm_{coat} during the aging scenarios (Fig. 8a). While the highest Rm_{coat} values were recorded during WL ($Rm_{coat} = 12.3$ at t_{96}) and SL (Rm_{coat} = 3.70 at t_{96}), the high-altitude scenarios demonstrated slower aging, with maximum Rm_{coat} values remaining below unity. According to Sedlacek et al. (2022), the ARCTEx Rmcoat values would correspond to real plume ages of less than a day. The slower mixing can be attributed to the absence of coagulation aging processes within AIDA compared to ambient conditions, where such processes pro-

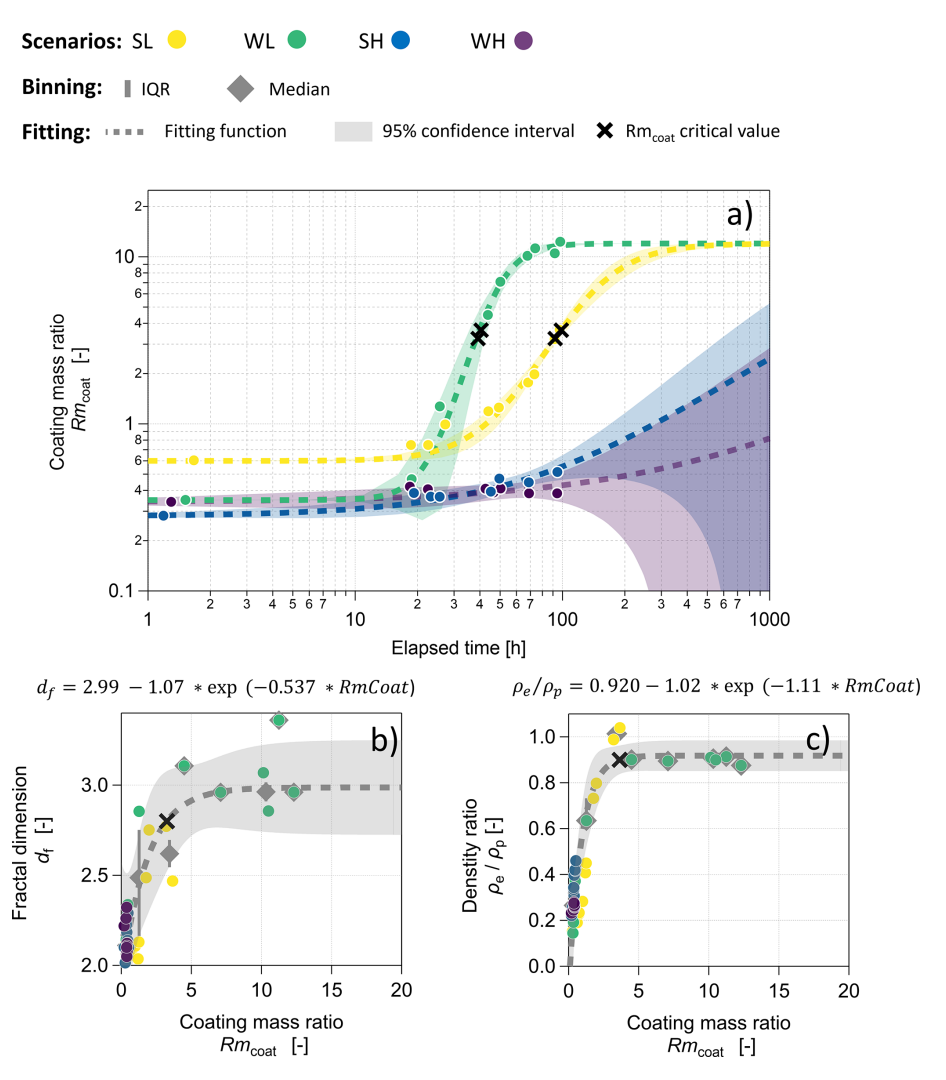


Figure 8. Comparison of the coating mass ratio (Rm_{coat}) with (a) experiment elapsed time; (b) fractal dimension, $d_{\rm f}$; (c) ratio of effective to particle density, $\rho_{\rm e}/\rho_{\rm p}$. All properties are calculated for particles with a mobility diameter of between 150–250 nm. ARCTEx scenarios: summer, low altitude (SL); winter, low altitude (WL); summer, high altitude (SH); winter, high altitude (WH). See text for details regarding the fitting functions.

mote quicker aging and thicker coatings (Matsui et al., 2013). To provide an aging timescale, we analyzed the relationship between Rm_{coat} and the fractal dimension (d_f ; Fig. 8b), as well as the ratio of the effective to particle density (ρ_e/ρ_p) ; Fig. 8c). Both properties are indicative of the sphericity or compaction of aerosol particles and were found to increase exponentially with Rmcoat, reaching an asymptotic maximum. These results reinforce the significant role of coating formation in influencing the sphericity of BC particles (Leung et al., 2017; Yuan et al., 2020). We aimed to identify a critical Rmcoat at which fractal BC restructures into a more compact shape. According to previous works that studied the variability of aerosol shape with fractal dimension (Olfert et al., 2007; Wang et al., 2017; Leskinen et al., 2023) and particle density (Rissler et al., 2014), we extrapolated Rm_{coat} corresponding to a $d_{\rm f}$ of 2.8 and to a $\rho_{\rm e}/\rho_{\rm p}$ of 0.9 based on

the exponential equations shown in Fig. 8. The so-derived critical Rm_{coat} of 3.24 and 3.64 marked the transition point at which fractal BC aggregates approached a spherical shape $(d_{\rm f}=2.8)$ and their observed material density $(\rho_{\rm e}/\rho_{\rm p}=0.9)$, respectively.

Next, we derived the aging timescale necessary to reach the critical coating mass for each scenario. We applied a Hill equation (Weiss, 1997; Goutelle et al., 2008) to model the non-linear relationship between Rm_{coat} and BC age, forcing the upper (maximum Rm_{coat} observed during WL) and lower (initial Rm_{coat} from each scenario) boundaries, along with a 95 % confidence interval (Fig. 8a, dashed lines). Compared to a more generic sigmoid equation, the Hill function allowed us to capture the sudden increase in Rm_{coat} in the early phase of the aging. From this fitted function, we derived the aging timescale corresponding to the critical Rm_{coat} range

(3.24–3.64, black crosses in Fig. 8). The critical Rm_{coat} was reached within the experimental time for both low-altitude scenarios, with the aging times quantified as 39–40 h for WL and 92–98 h for SL, corresponding to latitudes of 53–57 and 78–81° N, respectively. On the contrary, the coating formation rate was slower in the high-altitude experiments, with aging timescales exceeding the experiment duration, extrapolated to be 60-70 d for SH and over 600 d for WH. It is important to note that these aging timescales are subject to considerable uncertainty due to the fitting curve, as indicated by the wide confidence bands in Fig. 8a. Our experimental results reinforce the recent findings of Fierce et al. (2025), who highlighted the inadequacy of fixed aging timescales in models. Their work confirms that aging rates are regionally and seasonally dependent, as observed in the ARCTEx scenarios, significantly affecting simulated BC concentrations, particularly in the Arctic. Moreover, the altitudinal and seasonal aging patterns shown in Fig. 8 reflect ambient variability and lead to heterogeneous impacts on the hygroscopic and optical properties of BC (Jin et al., 2025)

4 Conclusions

The ARCTEx campaign aimed to quantify the aging timescale of BC particles during Arctic transport by simulating quasi-real conditions derived from reanalysis data in the AIDA chamber. The chamber successfully reproduced the meteorological and chemical conditions of four distinct transport scenarios, with a focus on nitrate and organics, aging, and sustained aging experiments for up to 115 h.

The fundamental physical properties of BC showed a distinct temporal evolution depending on the simulated environmental conditions. Temperature proved to be a critical factor controlling the evolution of BC properties until the end of the transport (~110-120 h, 90° N). High-altitude experiments conducted at low temperatures $(-59 \,^{\circ}\text{C} < T < -35 \,^{\circ}\text{C})$ exhibited minimal changes in mixing state and morphology, characterized by a final coating mass fraction of 25 %-30 %, a coating thickness of 5-10 nm, a fractal dimension of 2.0-2.4, and an effective density of $400-800 \,\mathrm{kg} \,\mathrm{m}^{-3}$. In contrast, low-altitude experiments conducted at higher temperatures $(-22 \,{}^{\circ}\text{C} < T < 21 \,{}^{\circ}\text{C})$ resulted in significant internal mixing and compaction. These scenarios yielded a final coating mass fraction of 78 %-97 %, a coating thickness of 40-60 nm, a fractal dimension of 2.8-3.0, and an effective density of $1300-1500 \,\mathrm{kg}\,\mathrm{m}^{-3}$. Notably, summer conditions with positive temperatures, extended irradiation, and limited nitrogen oxide availability favored the formation of organic coatings compared to winter, where nitrate coatings were dominant.

This study successfully quantified the time required to transform fresh, externally mixed, fractal BC particles into aged, internally mixed, and compact particles across the four scenarios. The fastest aging was observed in winter at low altitudes, where particles became fully coated within 39–40 h

after emission, corresponding to latitudes of $53-57^{\circ}$ N. In summer, at low altitudes, the aging timescale was slightly longer, ranging from 92 to 98 h and corresponding to latitudes of $78-81^{\circ}$ N. In contrast, high-altitude transport scenarios were characterized by aging timescales exceeding the experiment duration (120 h) and reaching the northernmost latitude (90° N) independently from the season.

For the first time, reanalysis data were used to drive extended aging experiments in a simulation chamber replicating Arctic transport, enabling the evaluation of aging effects on BC's fundamental properties. Hence, our work indicates that the aging timescale and impacts on fundamental BC properties vary dramatically as a function of the altitude and season of transport. These experimentally derived timescales and transformation pathways provide crucial input for constraining BC aging parameterizations in models, helping to bridge the gap between laboratory-scale studies and realworld Arctic conditions. In forthcoming work, we will discuss the implications of this temporal evolution on climaterelevant properties, such as light absorption and activation as cloud droplets and ice crystals. Together, these studies aim to support the modeling community in improving the representation of BC aging processes in transport simulations, ultimately enhancing the accuracy of climate projections.

Appendix A

Table A1. List of abbreviations, described properties, units, types (M denotes measured, C denotes calculated through the merging of different measurements, and A denotes assumed), and measuring instruments or sources.

Symbol	Property	Unit	Type	Instrument/source
d_{f}	Particle fractal exponent	_	С	DMA-APM
$D_{ extsf{p-DMA}}$	Particle mobility diameter	nm	M	SMPS
$D_{\text{Np-GM}}$	Geometric mean of the number size distribution of total particles	nm	M	SMPS
$D_{\text{NrBC-GM}}$	Geometric mean of the number size distribution of rBC	nm	M	SP2
$D_{ m ve-p}$	Particle volume-equivalent diameter	nm	C	DMA-APM-SP2/AMS
$D_{\text{ve-rBC}}$	rBC particle volume-equivalent diameter	nm	M	SP2
Fm _{coat}	Coating mass fraction	_	C	DMA-APM-SP2
Fm_{rBC}	rBC mass fraction	_	C	DMA-APM-SP2
FM_{nit}	Nitrate mass concentration fraction	_	M	AMS
FMorg	Organic mass concentration fraction	_	M	AMS
GF_{Dp}	Growth factor of $D_{\text{Np-GM}}$	_	C	SMPS
GF_{DrBC}	Growth factor of $D_{NrBC-GM}$	_	C	SP2
GR_{Dp}	Growth rate of $D_{\text{Np-GM}}$	_	C	SMPS
GR_{DrBC}	Growth rate of $D_{NrBC-GM}$	_	C	SP2
$k_{\mathbf{f}}$	Fractal constant	_	C	DMA-APM
$M_{ m rBC}$	rBC particle mass concentration	${\rm ngm^{-3}}$	M	SP2
$M_{\text{p-SMPS}}$	Mass concentration of total particles derived from SMPS		C	SMPS
$M_{\text{p-SP2}}$	Mass concentration of total particles derived from SP2		C	SP2
$m_{\text{p-APM}}$	Single-particle mass	fg	M	APM
$N_{\rm rBC}$	Number concentration of rBC particles	cm^{-3}	M	SP2
$\Delta D_{ m ve}$	Volume-equivalent coating thickness	nm	C	DMA-APM-SP2/AMS
ρ_{BC}	BC core material density	${\rm kg}{\rm m}^{-3}$	A	Yon et al. (2015)
ρe	Effective density	$kg m^{-3}$	C	DMA-APM
$\rho_{\rm coat}$	Coating-material density	${\rm kg}{\rm m}^{-3}$	C	AMS
$ ho_{ m p}$	Particle density	${\rm kg}{\rm m}^{-3}$	C	DMA-APM-SP2/AMS
$\rho_{ m nit}$	Nitrate-material density	${\rm kg}{\rm m}^{-3}$	A	Pokorná et al. (2022)
$\rho_{ m org}$	Organic-material density	${\rm kg}{\rm m}^{-3}$	A	Lim and Turpin (2002)
Rm _{coat}	Ratio of coating over rBC core mass	-	C	DMA-APM-SP2

Data availability. The reanalysis data used to characterize the meteorological transport conditions in this study are publicly available through the Copernicus Climate Data Store (ERA5 monthly averaged data on pressure levels from 1940 to present): https://doi.org/10.24381/cds.6860a573 (Hersbach et al., 2023). The reanalysis data used to characterize the chemical transport conditions in this study are publicly available through the Atmosphere Data Store (CAMS global reanalysis (EAC4) monthly averaged fields): https://doi.org/10.24381/fd75fff2 (Copernicus Atmosphere Monitoring Service, 2020). All data acquired during the ARCTEx experiments in the AIDA chamber are publicly available on the KITopen RADAR repository: https://doi.org/10.35097/7gh3j1jzabrzkcx9 (Zanatta et al., 2025).

Supplement. The supplement related to this article is available online at https://doi.org/10.5194/ar-3-477-2025-supplement.

Author contributions. MZ conceived the project, conducted the microphysics measurements, and wrote the paper. OM, HS, RW, FV, and AH contributed to the design of the experiments. PB, YG, NU, and FV performed the measurements of the ice-nucleating particles. CL and MS performed the optical measurements. YH, FJ, and YL performed the aerosol chemistry measurements. PG and PL provided the single-particle soot photometer. All of the authors contributed equally to the writing of the paper.

Competing interests. The contact author has declared that none of the authors has any competing interests.

Disclaimer. Publisher's note: Copernicus Publications remains neutral with regard to jurisdictional claims made in the text, published maps, institutional affiliations, or any other geographical representation in this paper. While Copernicus Publications makes every effort to include appropriate place names, the final responsibil-

ity lies with the authors. Views expressed in the text are those of the authors and do not necessarily reflect the views of the publisher.

Acknowledgements. The authors gratefully acknowledge the support of the AIDA (Aerosol Interaction and Dynamics in the Atmosphere) facility team at Karlsruhe Institute of Technology (KIT).

Financial support. This research has been funded by the Deutsche Forschungsgemeinschaft (grant no. 457895178). Marco Zanatta was partially supported by the ITINERIS project (no. IR0000032, D.D. no. 130/2022 – CUP B53C22002150006), funded by the EU – Next Generation EU PNRR-Mission 4 "Education and Research".

Review statement. This paper was edited by Attila Nagy and reviewed by three anonymous referees.

References

- Alexander, B., Hastings, M. G., Allman, D. J., Dachs, J., Thornton, J. A., and Kunasek, S. A.: Quantifying atmospheric nitrate formation pathways based on a global model of the oxygen isotopic composition (Δ¹⁷O) of atmospheric nitrate, Atmos. Chem. Phys., 9, 5043–5056, https://doi.org/10.5194/acp-9-5043-2009, 2009.
- Alexander, B., Sherwen, T., Holmes, C. D., Fisher, J. A., Chen, Q., Evans, M. J., and Kasibhatla, P.: Global inorganic nitrate production mechanisms: comparison of a global model with nitrate isotope observations, Atmos. Chem. Phys., 20, 3859–3877, https://doi.org/10.5194/acp-20-3859-2020, 2020.
- AMAP: AMAP Assessment 2021: Impacts of Short-lived Climate Forcers on Arctic Climate, Air Quality, and Human Health, ISBN 978-82-7971-202-2, 2021.
- Anderson, T. L. and Ogren, J. A.: Determining Aerosol Radiative Properties Using the TSI 3563 Integrating Nephelometer, Aerosol Sci. Technol., 29, 57–69, https://doi.org/10.1080/02786829808965551, 1998.
- Backman, J., Schmeisser, L., and Asmi, E.: Asian Emissions Explain Much of the Arctic Black Carbon Events, Geophys. Res. Lett., 48, e2020GL091913, https://doi.org/10.1029/2020GL091913, 2021.
- Bambha, R. P., Dansson, M. A., Schrader, P. E., and Michelsen, H. A.: Effects of volatile coatings and coating removal mechanisms on the morphology of graphitic soot, Carbon, 61, 80–96, https://doi.org/10.1016/j.carbon.2013.04.070, 2013.
- Barrie, L. A.: Arctic air pollution: An overview of current knowledge, Atmos. Environ., 20, 643–663, https://doi.org/10.1016/0004-6981(86)90180-0, 1986.
- Bertozzi, B., Wagner, R., Song, J., Höhler, K., Pfeifer, J., Saathoff, H., Leisner, T., and Möhler, O.: Ice nucleation ability of ammonium sulfate aerosol particles internally mixed with secondary organics, Atmos. Chem. Phys., 21, 10779–10798, https://doi.org/10.5194/acp-21-10779-2021, 2021.
- Bond, T. C., Doherty, S. J., Fahey, D. W., Forster, P. M., Berntsen, T., DeAngelo, B. J., Flanner, M. G., Ghan, S., Kärcher, B., Koch,

- D., Kinne, S., Kondo, Y., Quinn, P. K., Sarofim, M. C., Schultz, M. G., Schulz, M., Venkataraman, C., Zhang, H., Zhang, S., Bellouin, N., Guttikunda, S. K., Hopke, P. K., Jacobson, M. Z., Kaiser, J. W., Klimont, Z., Lohmann, U., Schwarz, J. P., Shindell, D., Storelvmo, T., Warren, S. G., and Zender, C. S.: Bounding the role of black carbon in the climate system: A scientific assessment, J. Geophys. Res. Atmospheres, 118, 5380–5552, https://doi.org/10.1002/jgrd.50171, 2013.
- Bozzo, A., Remy, S., Benedetti, A., Flemming, J., Bechtold, P., Rodwell, M., and Morcrette, J. J.: Implementation of a CAMS-based aerosol climatology in the IFS, ECMWF, https://www.ecmwf.int/sites/default/files/elibrary/2017/ 17219-implementation-cams-based-aerosol-climatology-ifs.pdf (last access: 22 October 2025), 2017.
- Burrows, S. M., McCluskey, C. S., Cornwell, G., Steinke, I., Zhang, K., Zhao, B., Zawadowicz, M., Raman, A., Kulkarni, G., China, S., Zelenyuk, A., and DeMott, P. J.: Ice-Nucleating Particles That Impact Clouds and Climate: Observational and Modeling Research Needs, Rev. Geophys., 60, e2021RG000745, https://doi.org/10.1029/2021RG000745, 2022.
- Canagaratna, M. R., Jimenez, J. L., Kroll, J. H., Chen, Q., Kessler, S. H., Massoli, P., Hildebrandt Ruiz, L., Fortner, E., Williams, L. R., Wilson, K. R., Surratt, J. D., Donahue, N. M., Jayne, J. T., and Worsnop, D. R.: Elemental ratio measurements of organic compounds using aerosol mass spectrometry: characterization, improved calibration, and implications, Atmos. Chem. Phys., 15, 253–272, https://doi.org/10.5194/acp-15-253-2015, 2015.
- Cappa, C. D., Onasch, T. B., Massoli, P., Worsnop, D. R., Bates, T. S., Cross, E. S., Davidovits, P., Hakala, J., Hayden, K. L., Jobson, B. T., Kolesar, K. R., Lack, D. A., Lerner, B. M., Li, S.-M., Mellon, D., Nuaaman, I., Olfert, J. S., Petäjä, T., Quinn, P. K., Song, C., Subramanian, R., Williams, E. J., and Zaveri, R. A.: Radiative Absorption Enhancements Due to the Mixing State of Atmospheric Black Carbon, Science, 337, 1078–1081, https://doi.org/10.1126/science.1223447, 2012.
- Chang, W. L., Bhave, P. V., Brown, S. S., Riemer, N., Stutz, J., and Dabdub, D.: Heterogeneous Atmospheric Chemistry, Ambient Measurements, and Model Calculations of N_2O_5 : A Review, Aerosol Sci. Technol., 45, 665–695, https://doi.org/10.1080/02786826.2010.551672, 2011.
- Chen, G., Liu, C., Wang, J., Yin, Y., and Wang, Y.: Accounting for Black Carbon Mixing State, Nonsphericity, and Heterogeneity Effects in Its Optical Property Parameterization in a Climate Model, J. Geophys. Res. Atmospheres, 129, e2024JD041135, https://doi.org/10.1029/2024JD041135, 2024.
- Copernicus Atmosphere Monitoring Service: CAMS global reanalysis (EAC4) monthly averaged fields, Copernicus Atmosphere Monitoring Service (CAMS) Atmosphere Data Store [data set], https://doi.org/10.24381/fd75fff2, 2020.
- Corbin, J. C., Modini, R. L., and Gysel-Beer, M.: Mechanisms of soot-aggregate restructuring and compaction, Aerosol Sci. Technol., 57, 89–111, https://doi.org/10.1080/02786826.2022.2137385, 2023.
- Cross, E. S., Onasch, T. B., Ahern, A., Wrobel, W., Slowik, J. G.,
 Olfert, J., Lack, D. A., Massoli, P., Cappa, C. D., Schwarz, J.
 P., Spackman, J. R., Fahey, D. W., Sedlacek, A., Trimborn, A.,
 Jayne, J. T., Freedman, A., Williams, L. R., Ng, N. L., Mazzoleni,
 C., Dubey, M., Brem, B., Kok, G., Subramanian, R., Freitag, S.,
 Clarke, A., Thornhill, D., Marr, L. C., Kolb, C. E., Worsnop, D.

- R., and Davidovits, P.: Soot Particle Studies Instrument Inter-Comparison Project Overview, Aerosol Sci. Technol., 44, 592–611, https://doi.org/10.1080/02786826.2010.482113, 2010.
- Dahlkötter, F., Gysel, M., Sauer, D., Minikin, A., Baumann, R., Seifert, P., Ansmann, A., Fromm, M., Voigt, C., and Weinzierl, B.: The Pagami Creek smoke plume after long-range transport to the upper troposphere over Europe aerosol properties and black carbon mixing state, Atmos. Chem. Phys., 14, 6111–6137, https://doi.org/10.5194/acp-14-6111-2014, 2014.
- Dalirian, M., Ylisirniö, A., Buchholz, A., Schlesinger, D., Ström, J., Virtanen, A., and Riipinen, I.: Cloud droplet activation of black carbon particles coated with organic compounds of varying solubility, Atmos. Chem. Phys., 18, 12477–12489, https://doi.org/10.5194/acp-18-12477-2018, 2018.
- Daoudi, M., Schiffmann, P., Faccinetto, A., Frobert, A., and Desgroux, P.: Comprehensive characterization of particulate matter emissions produced by a liquid-fueled miniCAST burner, Aerosol Sci. Technol., 57, 872–889, https://doi.org/10.1080/02786826.2023.2228372, 2023.
- DeCarlo, P. F., Slowik, J. G., Worsnop, D. R., Davidovits, P., and Jimenez, J. L.: Particle Morphology and Density Characterization by Combined Mobility and Aerodynamic Diameter Measurements. Part 1: Theory, Aerosol Sci. Technol., 38, 1185–1205, https://doi.org/10.1080/027868290903907, 2004.
- DeCarlo, P. F., Kimmel, J. R., Trimborn, A., Northway, M. J., Jayne, J. T., Aiken, A. C., Gonin, M., Fuhrer, K., Horvath, T., Docherty, K. S., Worsnop, D. R., and Jimenez, J. L.: Field-Deployable, High-Resolution, Time-of-Flight Aerosol Mass Spectrometer, Anal. Chem., 78, 8281–8289, https://doi.org/10.1021/ac061249n, 2006.
- Ding, S. and Liu, D.: Evaluation of the CAMS reanalysis for atmospheric black carbon and carbon monoxide over the north China plain, Environ. Pollut., 314, 120286, https://doi.org/10.1016/j.envpol.2022.120286, 2022.
- Dorn, H.-P., Apodaca, R. L., Ball, S. M., Brauers, T., Brown, S. S., Crowley, J. N., Dubé, W. P., Fuchs, H., Häseler, R., Heitmann, U., Jones, R. L., Kiendler-Scharr, A., Labazan, I., Langridge, J. M., Meinen, J., Mentel, T. F., Platt, U., Pöhler, D., Rohrer, F., Ruth, A. A., Schlosser, E., Schuster, G., Shillings, A. J. L., Simpson, W. R., Thieser, J., Tillmann, R., Varma, R., Venables, D. S., and Wahner, A.: Intercomparison of NO₃ radical detection instruments in the atmosphere simulation chamber SAPHIR, Atmos. Meas. Tech., 6, 1111–1140, https://doi.org/10.5194/amt-6-1111-2013, 2013.
- Doussin, J.-F., Fuchs, H., Kiendler-Scharr, A., Seakins, P., and Wenger, J. (Eds.): A Practical Guide to Atmospheric Simulation Chambers, Springer International Publishing, Cham, https://doi.org/10.1007/978-3-031-22277-1, 2023.
- Dulitz, K., Amedro, D., Dillon, T. J., Pozzer, A., and Crowley, J. N.: Temperature-(208–318 K) and pressure-(18–696 Torr) dependent rate coefficients for the reaction between OH and HNO₃, Atmos. Chem. Phys., 18, 2381–2394, https://doi.org/10.5194/acp-18-2381-2018, 2018.
- Ehara, K., Hagwood, C., and Coakley, K. J.: Novel method to classify aerosol particles according to their mass-to-charge ratio Aerosol particle mass analyser, J. Aerosol Sci., 27, 217–234, https://doi.org/10.1016/0021-8502(95)00562-5, 1996.
- Ess, M. N. and Vasilatou, K.: Characterization of a new mini-CAST with diffusion flame and premixed flame options:

- Generation of particles with high EC content in the size range 30 nm to 200 nm, Aerosol Sci. Technol., 53, 29–44, https://doi.org/10.1080/02786826.2018.1536818, 2019.
- Ess, M. N., Bertò, M., Irwin, M., Modini, R. L., Gysel-Beer, M., and Vasilatou, K.: Optical and morphological properties of soot particles generated by the miniCAST 5201 BC generator, Aerosol Sci. Technol., 55, 828–847, https://doi.org/10.1080/02786826.2021.1901847, 2021.
- Fahey, D. W., Gao, R.-S., Möhler, O., Saathoff, H., Schiller, C., Ebert, V., Krämer, M., Peter, T., Amarouche, N., Avallone, L. M., Bauer, R., Bozóki, Z., Christensen, L. E., Davis, S. M., Durry, G., Dyroff, C., Herman, R. L., Hunsmann, S., Khaykin, S. M., Mackrodt, P., Meyer, J., Smith, J. B., Spelten, N., Troy, R. F., Vömel, H., Wagner, S., and Wienhold, F. G.: The AquaVIT-1 intercomparison of atmospheric water vapor measurement techniques, Atmos. Meas. Tech., 7, 3177–3213, https://doi.org/10.5194/amt-7-3177-2014, 2014.
- Fierce, L., Onasch, T. B., Cappa, C. D., Mazzoleni, C., China, S., Bhandari, J., Davidovits, P., Fischer, D. A., Helgestad, T., Lambe, A. T., Sedlacek, A. J., Smith, G. D., and Wolff, L.: Radiative absorption enhancements by black carbon controlled by particle-to-particle heterogeneity in composition, Proc. Natl. Acad. Sci., 117, 5196–5203, https://doi.org/10.1073/pnas.1919723117, 2020.
- Fierce, L., Li, Y., Feng, Y., Riemer, N., Schutgens, N. A. J., Aiken, A. C., Dubey, M. K., Ma, P.-L., and Wuebbles, D.: Constraining Black Carbon Aging in Global Models to Reflect Timescales for Internal Mixing, J. Adv. Model. Earth Syst., 17, e2024MS004471, https://doi.org/10.1029/2024MS004471, 2025.
- Friebel, F. and Mensah, A. A.: Ozone Concentration versus Temperature: Atmospheric Aging of Soot Particles, Langmuir, 35, 14437–14450, https://doi.org/10.1021/acs.langmuir.9b02372, 2019.
- Gao, L., Song, J., Mohr, C., Huang, W., Vallon, M., Jiang, F., Leisner, T., and Saathoff, H.: Kinetics, SOA yields, and chemical composition of secondary organic aerosol from β-caryophyllene ozonolysis with and without nitrogen oxides between 213 and 313 K, Atmos. Chem. Phys., 22, 6001–6020, https://doi.org/10.5194/acp-22-6001-2022, 2022.
- Gao, R. S., Schwarz, J. P., Kelly, K. K., Fahey, D. W., Watts, L. A., Thompson, T. L., Spackman, J. R., Slowik, J. G., Cross, E. S., Han, J.-H., Davidovits, P., Onasch, T. B., and Worsnop, D. R.: A Novel Method for Estimating Light-Scattering Properties of Soot Aerosols Using a Modified Single-Particle Soot Photometer, Aerosol Sci. Technol., 41, 125–135, https://doi.org/10.1080/02786820601118398, 2007.
- Goutelle, S., Maurin, M., Rougier, F., Barbaut, X., Bourguignon, L., Ducher, M., and Maire, P.: The Hill equation: a review of its capabilities in pharmacological modelling, Fundam. Clin. Pharmacol., 22, 633–648, https://doi.org/10.1111/j.1472-8206.2008.00633.x, 2008.
- Graham, R. M., Hudson, S. R., and Maturilli, M.: Improved Performance of ERA5 in Arctic Gateway Relative to Four Global Atmospheric Reanalyses, Geophys. Res. Lett., 46, 6138–6147, https://doi.org/10.1029/2019GL082781, 2019.
- Gysel, M., Laborde, M., Olfert, J. S., Subramanian, R., and Gröhn, A. J.: Effective density of Aquadag and fullerene soot black carbon reference materials used for SP2 calibration, Atmos. Meas.

- Tech., 4, 2851–2858, https://doi.org/10.5194/amt-4-2851-2011, 2011
- Gysel, M., Laborde, M., Mensah, A. A., Corbin, J. C., Keller, A., Kim, J., Petzold, A., and Sierau, B.: Technical Note: The single particle soot photometer fails to reliably detect PALAS soot nanoparticles, Atmos. Meas. Tech., 5, 3099–3107, https://doi.org/10.5194/amt-5-3099-2012, 2012.
- Henning, S., Ziese, M., Kiselev, A., Saathoff, H., Möhler, O., Mentel, T. F., Buchholz, A., Spindler, C., Michaud, V., Monier, M., Sellegri, K., and Stratmann, F.: Hygroscopic growth and droplet activation of soot particles: uncoated, succinic or sulfuric acid coated, Atmos. Chem. Phys., 12, 4525–4537, https://doi.org/10.5194/acp-12-4525-2012, 2012.
- Hersbach, H., Bell, B., Berrisford, P., Hirahara, S., Horányi, A., Muñoz-Sabater, J., Nicolas, J., Peubey, C., Radu, R., Schepers, D., Simmons, A., Soci, C., Abdalla, S., Abellan, X., Balsamo, G., Bechtold, P., Biavati, G., Bidlot, J., Bonavita, M., De Chiara, G., Dahlgren, P., Dee, D., Diamantakis, M., Dragani, R., Flemming, J., Forbes, R., Fuentes, M., Geer, A., Haimberger, L., Healy, S., Hogan, R. J., Hólm, E., Janisková, M., Keeley, S., Laloyaux, P., Lopez, P., Lupu, C., Radnoti, G., de Rosnay, P., Rozum, I., Vamborg, F., Villaume, S., and Thépaut, J.-N.: The ERA5 global reanalysis, Q. J. R. Meteorol. Soc., 146, 1999–2049, https://doi.org/10.1002/qj.3803, 2020.
- Hersbach, H., Bell, B., Berrisford, P., Biavati, G., Horányi, A., Muñoz Sabater, J., Nicolas, J., Peubey, C., Radu, R., Rozum, I., Schepers, D., Simmons, A., Soci, C., Dee, D., and Thépaut, J.-N.: ERA5 monthly averaged data on pressure levels from 1940 to present, Copernicus Climate Change Service (C3S) Climate Data Store (CDS) [data set], https://doi.org/10.24381/cds.6860a573, 2023.
- Heuser, J., Di Biagio, C., Yon, J., Cazaunau, M., Bergé, A., Pangui, E., Zanatta, M., Renzi, L., Marinoni, A., Inomata, S., Yu, C., Bernardoni, V., Chevaillier, S., Ferry, D., Laj, P., Maillé, M., Massabò, D., Mazzei, F., Noyalet, G., Tanimoto, H., Temime-Roussel, B., Vecchi, R., Vernocchi, V., Formenti, P., Picquet-Varrault, B., and Doussin, J.-F.: Spectral optical properties of soot: laboratory investigation of propane flame particles and their link to composition, Atmos. Chem. Phys., 25, 6407–6428, https://doi.org/10.5194/acp-25-6407-2025, 2025.
- Inness, A., Ades, M., Agustí-Panareda, A., Barré, J., Benedictow, A., Blechschmidt, A.-M., Dominguez, J. J., Engelen, R., Eskes, H., Flemming, J., Huijnen, V., Jones, L., Kipling, Z., Massart, S., Parrington, M., Peuch, V.-H., Razinger, M., Remy, S., Schulz, M., and Suttie, M.: The CAMS reanalysis of atmospheric composition, Atmos. Chem. Phys., 19, 3515–3556, https://doi.org/10.5194/acp-19-3515-2019, 2019.
- Intergovernmental Panel On Climate Change (IPCC): Climate Change 2021 – The Physical Science Basis: Working Group I Contribution to the Sixth Assessment Report of the Intergovernmental Panel on Climate Change, 1st edn., Cambridge University Press, https://doi.org/10.1017/9781009157896, 2023.
- Jiang, F., Siemens, K., Linke, C., Li, Y., Gong, Y., Leisner, T., Laskin, A., and Saathoff, H.: Molecular analysis of secondary organic aerosol and brown carbon from the oxidation of indole, Atmos. Chem. Phys., 24, 2639–2649, https://doi.org/10.5194/acp-24-2639-2024, 2024.
- Jin, Y., Wang, J., Liu, C., Wong, D. C., Sarwar, G., Fahey, K. M., Wu, S., Wang, J., Cai, J., Tian, Z., Zhang, Z., Xing, J., Ding,

- A., and Wang, S.: Accounting for the black carbon aging process in a two-way coupled meteorology–air quality model, Atmos. Chem. Phys., 25, 2613–2630, https://doi.org/10.5194/acp-25-2613-2025, 2025.
- Jurányi, Z., Zanatta, M., Lund, M. T., Samset, B. H., Skeie, R. B., Sharma, S., Wendisch, M., and Herber, A.: Atmospheric concentrations of black carbon are substantially higher in spring than summer in the Arctic, Commun. Earth Environ., 4, 1–12, https://doi.org/10.1038/s43247-023-00749-x, 2023.
- Kanji, Z. A., Welti, A., Corbin, J. C., and Mensah, A. A.: Black Carbon Particles Do Not Matter for Immersion Mode Ice Nucleation, Geophys. Res. Lett., 47, e2019GL086764, https://doi.org/10.1029/2019GL086764, 2020.
- Khalizov, A. F., Xue, H., Wang, L., Zheng, J., and Zhang, R.: Enhanced Light Absorption and Scattering by Carbon Soot Aerosol Internally Mixed with Sulfuric Acid, J. Phys. Chem. A, 113, 1066–1074, https://doi.org/10.1021/jp807531n, 2009.
- Kim, S. C., Wang, J., Emery, M. S., Shin, W. G., Mulholland, G. W., and Pui, D. Y. H.: Structural Property Effect of Nanoparticle Agglomerates on Particle Penetration through Fibrous Filter, Aerosol Sci. Technol., https://doi.org/10.1080/02786820802653763, 2009.
- Knutson, E. O. and Whitby, K. T.: Aerosol classification by electric mobility: apparatus, theory, and applications, J. Aerosol Sci., 6, 443–451, https://doi.org/10.1016/0021-8502(75)90060-9, 1975.
- Koch, D., Schulz, M., Kinne, S., McNaughton, C., Spackman, J.
 R., Balkanski, Y., Bauer, S., Berntsen, T., Bond, T. C., Boucher, O., Chin, M., Clarke, A., De Luca, N., Dentener, F., Diehl, T., Dubovik, O., Easter, R., Fahey, D. W., Feichter, J., Fillmore, D., Freitag, S., Ghan, S., Ginoux, P., Gong, S., Horowitz, L., Iversen, T., Kirkevåg, A., Klimont, Z., Kondo, Y., Krol, M., Liu, X., Miller, R., Montanaro, V., Moteki, N., Myhre, G., Penner, J. E., Perlwitz, J., Pitari, G., Reddy, S., Sahu, L., Sakamoto, H., Schuster, G., Schwarz, J. P., Seland, Ø., Stier, P., Takegawa, N., Takemura, T., Textor, C., van Aardenne, J. A., and Zhao, Y.: Evaluation of black carbon estimations in global aerosol models, Atmos. Chem. Phys., 9, 9001–9026, https://doi.org/10.5194/acp-99001-2009, 2009.
- Kodros, J. K., Hanna, S. J., Bertram, A. K., Leaitch, W. R., Schulz, H., Herber, A. B., Zanatta, M., Burkart, J., Willis, M. D., Abbatt, J. P. D., and Pierce, J. R.: Size-resolved mixing state of black carbon in the Canadian high Arctic and implications for simulated direct radiative effect, Atmos. Chem. Phys., 18, 11345–11361, https://doi.org/10.5194/acp-18-11345-2018, 2018.
- Kostenidou, E., Pathak, R. K., and Pandis, S. N.: An Algorithm for the Calculation of Secondary Organic Aerosol Density Combining AMS and SMPS Data, Aerosol Sci. Technol., 41, 1002–1010, https://doi.org/10.1080/02786820701666270, 2007.
- Laborde, M., Mertes, P., Zieger, P., Dommen, J., Baltensperger, U., and Gysel, M.: Sensitivity of the Single Particle Soot Photometer to different black carbon types, Atmos. Meas. Tech., 5, 1031–1043, https://doi.org/10.5194/amt-5-1031-2012, 2012a.
- Laborde, M., Schnaiter, M., Linke, C., Saathoff, H., Naumann, K.H., Möhler, O., Berlenz, S., Wagner, U., Taylor, J. W., Liu, D.,
 Flynn, M., Allan, J. D., Coe, H., Heimerl, K., Dahlkötter, F.,
 Weinzierl, B., Wollny, A. G., Zanatta, M., Cozic, J., Laj, P.,
 Hitzenberger, R., Schwarz, J. P., and Gysel, M.: Single Particle
 Soot Photometer intercomparison at the AIDA chamber, Atmos.

- Meas. Tech., 5, 3077–3097, https://doi.org/10.5194/amt-5-3077-2012, 2012b
- Laborde, M., Crippa, M., Tritscher, T., Jurányi, Z., Decarlo, P. F., Temime-Roussel, B., Marchand, N., Eckhardt, S., Stohl, A., Baltensperger, U., Prévôt, A. S. H., Weingartner, E., and Gysel, M.: Black carbon physical properties and mixing state in the European megacity Paris, Atmos. Chem. Phys., 13, 5831–5856, https://doi.org/10.5194/acp-13-5831-2013, 2013.
- Lefevre, G., Yon, J., Bouvier, M., Liu, F., and Coppalle, A.: Impact of Organic Coating on Soot Angular and Spectral Scattering Properties, Env. Sci. Technol., 53, 6383–6391, https://doi.org/10.1021/acs.est.8b05482, 2019.
- Leskinen, J., Hartikainen, A., Väätäinen, S., Ihalainen, M., Virkkula, A., Mesceriakovas, A., Tiitta, P., Miettinen, M., Lamberg, H., Czech, H., Yli-Pirilä, P., Tissari, J., Jakobi, G., Zimmermann, R., and Sippula, O.: Photochemical Aging Induces Changes in the Effective Densities, Morphologies, and Optical Properties of Combustion Aerosol Particles, Environ. Sci. Technol., 57, 5137–5148, https://doi.org/10.1021/acs.est.2c04151, 2023.
- Leung, K. K., Schnitzler, E. G., Dastanpour, R., Rogak, S. N., Jäger, W., and Olfert, J. S.: Relationship between Coating-Induced Soot Aggregate Restructuring and Primary Particle Number, Environ. Sci. Technol., 51, 8376–8383, https://doi.org/10.1021/acs.est.7b01140, 2017.
- Levy II, H., Moxim, W. J., Klonecki, A. A., and Kasibhatla, P. S.: Simulated tropospheric NO: Its evaluation, global distribution and individual source contributions, J. Geophys. Res. Atmospheres, 104, 26279–26306, https://doi.org/10.1029/1999JD900442, 1999.
- Li, F., Luo, B., Zhai, M., Liu, L., Zhao, G., Xu, H., Deng, T., Deng, X., Tan, H., Kuang, Y., and Zhao, J.: Black carbon content of traffic emissions significantly impacts black carbon mass size distributions and mixing states, Atmos. Chem. Phys., 23, 6545–6558, https://doi.org/10.5194/acp-23-6545-2023, 2023.
- Li, K., Chen, L., Han, K., Lv, B., Bao, K., Wu, X., Gao, X., and Cen, K.: Smog chamber study on aging of combustion soot in isoprene/SO₂/NO_x system: Changes of mass, size, effective density, morphology and mixing state, Atmos. Res., 184, 139–148, https://doi.org/10.1016/j.atmosres.2016.10.011, 2017.
- Li, W., Wang, Y., Yi, Z., Guo, B., Chen, W., Che, H., and Zhang, X.: Evaluation of MERRA-2 and CAMS reanalysis for black carbon aerosol in China, Environ. Pollut., 343, 123182, https://doi.org/10.1016/j.envpol.2023.123182, 2024a.
- Li, W., Riemer, N., Xu, L., Wang, Y., Adachi, K., Shi, Z., Zhang, D., Zheng, Z., and Laskin, A.: Microphysical properties of atmospheric soot and organic particles: measurements, modeling, and impacts, Npj Clim. Atmos. Sci., 7, 1–14, https://doi.org/10.1038/s41612-024-00610-8, 2024b.
- Lim, C. Y., Hagan, D. H., Coggon, M. M., Koss, A. R., Sekimoto, K., de Gouw, J., Warneke, C., Cappa, C. D., and Kroll, J. H.: Secondary organic aerosol formation from the laboratory oxidation of biomass burning emissions, Atmos. Chem. Phys., 19, 12797– 12809, https://doi.org/10.5194/acp-19-12797-2019, 2019.
- Lim, H.-J. and Turpin, B. J.: Origins of Primary and Secondary Organic Aerosol in Atlanta: Results of Time-Resolved Measurements during the Atlanta Supersite Experiment, Environ. Sci. Technol., 36, 4489–4496, https://doi.org/10.1021/es0206487, 2002.

- Linke, C., Ibrahim, I., Schleicher, N., Hitzenberger, R., Andreae, M. O., Leisner, T., and Schnaiter, M.: A novel single-cavity three-wavelength photoacoustic spectrometer for atmospheric aerosol research, Atmos. Meas. Tech., 9, 5331–5346, https://doi.org/10.5194/amt-9-5331-2016, 2016.
- Liu, P. S. K., Deng, R., Smith, K. A., Williams, L. R., Jayne, J. T., Canagaratna, M. R., Moore, K., Onasch, T. B., Worsnop, D. R., and Deshler, T.: Transmission Efficiency of an Aerodynamic Focusing Lens System: Comparison of Model Calculations and Laboratory Measurements for the Aerodyne Aerosol Mass Spectrometer, Aerosol Sci. Technol., 41, 721–733, https://doi.org/10.1080/02786820701422278, 2007.
- Liu, X., Ma, P.-L., Wang, H., Tilmes, S., Singh, B., Easter, R. C., Ghan, S. J., and Rasch, P. J.: Description and evaluation of a new four-mode version of the Modal Aerosol Module (MAM4) within version 5.3 of the Community Atmosphere Model, Geosci. Model Dev., 9, 505–522, https://doi.org/10.5194/gmd-9-505-2016, 2016.
- Lund, M. T. and Berntsen, T.: Parameterization of black carbon aging in the OsloCTM2 and implications for regional transport to the Arctic, Atmos. Chem. Phys., 12, 6999–7014, https://doi.org/10.5194/acp-12-6999-2012, 2012.
- Lund, M. T., Samset, B. H., Skeie, R. B., Watson-Parris, D., Katich, J. M., Schwarz, J. P., and Weinzierl, B.: Short Black Carbon lifetime inferred from a global set of aircraft observations, Npj Clim. Atmos. Sci., 1, 1–8, https://doi.org/10.1038/s41612-018-0040-x, 2018.
- Mahmood, R., von Salzen, K., Flanner, M., Sand, M., Langner, J., Wang, H., and Huang, L.: Seasonality of global and Arctic black carbon processes in the Arctic Monitoring and Assessment Programme models, J. Geophys. Res. Atmospheres, 121, 7100–7116, https://doi.org/10.1002/2016JD024849, 2016.
- Mamakos, A., Khalek, I., Giannelli, R., and Spears, M.: Characterization of Combustion Aerosol Produced by a Mini-CAST and Treated in a Catalytic Stripper, Aerosol Sci. Technol., 47, 927–936, https://doi.org/10.1080/02786826.2013.802762, 2013.
- Maricq, M. M.: Coagulation dynamics of fractal-like soot aggregates, J. Aerosol Sci., 38, 141–156, https://doi.org/10.1016/j.jaerosci.2006.11.004, 2007.
- Maricq, M. M.: Examining the Relationship Between Black Carbon and Soot in Flames and Engine Exhaust, Aerosol Sci. Technol., 48, 620–629, https://doi.org/10.1080/02786826.2014.904961, 2014.
- Mason, Y. C., Schoonraad, G.-L., Orasche, J., Bisig, C., Jakobi, G., Zimmermann, R., and Forbes, P. B. C.: Comparative sampling of gas phase volatile and semi-volatile organic fuel emissions from a combustion aerosol standard system, Environ. Technol. Innov., 19, 100945, https://doi.org/10.1016/j.eti.2020.100945, 2020.
- Massling, A., Nielsen, I. E., Kristensen, D., Christensen, J. H., Sørensen, L. L., Jensen, B., Nguyen, Q. T., Nøjgaard, J. K., Glasius, M., and Skov, H.: Atmospheric black carbon and sulfate concentrations in Northeast Greenland, Atmos. Chem. Phys., 15, 9681–9692, https://doi.org/10.5194/acp-15-9681-2015, 2015.
- Matsui, H.: Black carbon simulations using a size- and mixingstate-resolved three-dimensional model: 2. Aging timescale and its impact over East Asia, J. Geophys. Res. Atmospheres, 121, 2015JD023999, https://doi.org/10.1002/2015JD023999, 2016.
- Matsui, H., Koike, M., Kondo, Y., Moteki, N., Fast, J. D., and Zaveri, R. A.: Development and validation of a black car-

- bon mixing state resolved three-dimensional model: Aging processes and radiative impact: BC Mixing State Resolved WRF-CHEM, J. Geophys. Res. Atmospheres, 118, 2304–2326, https://doi.org/10.1029/2012JD018446, 2013.
- Matsumi, Y., Comes, F. J., Hancock, G., Hofzumahaus, A., Hynes, A. J., Kawasaki, M., and Ravishankara, A. R.: Quantum yields for production of O(1D) in the ultraviolet photolysis of ozone: Recommendation based on evaluation of laboratory data, J. Geophys. Res. Atmospheres, 107, ACH 1-1–ACH 1-12, https://doi.org/10.1029/2001JD000510, 2002.
- McCarty, J. L., Aalto, J., Paunu, V.-V., Arnold, S. R., Eckhardt, S., Klimont, Z., Fain, J. J., Evangeliou, N., Venäläinen, A., Tchebakova, N. M., Parfenova, E. I., Kupiainen, K., Soja, A. J., Huang, L., and Wilson, S.: Reviews and syntheses: Arctic fire regimes and emissions in the 21st century, Biogeosciences, 18, 5053–5083, https://doi.org/10.5194/bg-18-5053-2021, 2021.
- McMeeking, G. R., Hamburger, T., Liu, D., Flynn, M., Morgan, W. T., Northway, M., Highwood, E. J., Krejci, R., Allan, J. D., Minikin, A., and Coe, H.: Black carbon measurements in the boundary layer over western and northern Europe, Atmos. Chem. Phys., 10, 9393–9414, https://doi.org/10.5194/acp-10-9393-2010, 2010.
- Middlebrook, A. M., Bahreini, R., Jimenez, J. L., and Canagaratna, M. R.: Evaluation of Composition-Dependent Collection Efficiencies for the Aerodyne Aerosol Mass Spectrometer using Field Data, Aerosol Sci. Technol., 46, 258–271, https://doi.org/10.1080/02786826.2011.620041, 2012.
- Möhler, O., Stetzer, O., Schaefers, S., Linke, C., Schnaiter, M., Tiede, R., Saathoff, H., Krämer, M., Mangold, A., Budz, P., Zink, P., Schreiner, J., Mauersberger, K., Haag, W., Kärcher, B., and Schurath, U.: Experimental investigation of homogeneous freezing of sulphuric acid particles in the aerosol chamber AIDA, Atmos. Chem. Phys., 3, 211–223, https://doi.org/10.5194/acp-3-211-2003, 2003.
- Möhler, O., Büttner, S., Linke, C., Schnaiter, M., Saathoff, H., Stetzer, O., Wagner, R., Krämer, M., Mangold, A., Ebert, V., and Schurath, U.: Effect of sulfuric acid coating on heterogeneous ice nucleation by soot aerosol particles, J. Geophys. Res. Atmospheres, 110, https://doi.org/10.1029/2004JD005169, 2005.
- Moore, R. H., Ziemba, L. D., Dutcher, D., Beyersdorf, A. J., Chan, K., Crumeyrolle, S., Raymond, T. M., Thornhill, K. L., Winstead, E. L., and Anderson, B. E.: Mapping the Operation of the Miniature Combustion Aerosol Standard (Mini-CAST) Soot Generator, Aerosol Sci. Technol., 48, 467–479, https://doi.org/10.1080/02786826.2014.890694, 2014.
- Morcrette, J.-J., Boucher, O., Jones, L., Salmond, D., Bechtold, P., Beljaars, A., Benedetti, A., Bonet, A., Kaiser, J. W., Razinger, M., Schulz, M., Serrar, S., Simmons, A. J., Sofiev, M., Suttie, M., Tompkins, A. M., and Untch, A.: Aerosol analysis and forecast in the European Centre for Medium-Range Weather Forecasts Integrated Forecast System: Forward modeling, J. Geophys. Res. Atmospheres, 114, https://doi.org/10.1029/2008JD011235, 2009.
- Moschos, V., Schmale, J., Aas, W., Becagli, S., Calzolai, G., Eleftheriadis, K., Moffett, C. E., Schnelle-Kreis, J., Severi, M., Sharma, S., Skov, H., Vestenius, M., Zhang, W., Hakola, H., Hellén, H., Huang, L., Jaffrezo, J.-L., Massling, A., Nøjgaard, J. K., Petäjä, T., Popovicheva, O., Sheesley, R. J., Traversi, R., Yttri, K. E., Prévôt, A. S. H., Baltensperger, U., and Haddad, I. E.: Elucidating the present-day chemical composi-

- tion, seasonality and source regions of climate-relevant aerosols across the Arctic land surface, Environ. Res. Lett., 17, 034032, https://doi.org/10.1088/1748-9326/ac444b, 2022.
- Moteki, N. and Kondo, Y.: Dependence of Laser-Induced Incandescence on Physical Properties of Black Carbon Aerosols: Measurements and Theoretical Interpretation, Aerosol Sci. Technol., 44, 663–675, https://doi.org/10.1080/02786826.2010.484450, 2010.
- Naseri, A., Sipkens, T. A., Rogak, S. N., and Olfert, J. S.: Optimized instrument configurations for tandem particle mass analyzer and single particle-soot photometer experiments, J. Aerosol Sci., 160, 105897, https://doi.org/10.1016/j.jaerosci.2021.105897, 2022.
- Naumann, K.-H.: COSIMA a computer program simulating the dynamics of fractal aerosols, J. Aerosol Sci., 34, 1371–1397, https://doi.org/10.1016/S0021-8502(03)00367-7, 2003.
- Ng, N. L., Brown, S. S., Archibald, A. T., Atlas, E., Cohen, R. C., Crowley, J. N., Day, D. A., Donahue, N. M., Fry, J. L., Fuchs, H., Griffin, R. J., Guzman, M. I., Herrmann, H., Hodzic, A., Iinuma, Y., Jimenez, J. L., Kiendler-Scharr, A., Lee, B. H., Luecken, D. J., Mao, J., McLaren, R., Mutzel, A., Osthoff, H. D., Ouyang, B., Picquet-Varrault, B., Platt, U., Pye, H. O. T., Rudich, Y., Schwantes, R. H., Shiraiwa, M., Stutz, J., Thornton, J. A., Tilgner, A., Williams, B. J., and Zaveri, R. A.: Nitrate radicals and biogenic volatile organic compounds: oxidation, mechanisms, and organic aerosol, Atmos. Chem. Phys., 17, 2103–2162, https://doi.org/10.5194/acp-17-2103-2017, 2017.
- Olfert, J. S., Symonds, J. P. R., and Collings, N.: The effective density and fractal dimension of particles emitted from a light-duty diesel vehicle with a diesel oxidation catalyst, J. Aerosol Sci., 38, 69–82, https://doi.org/10.1016/j.jaerosci.2006.10.002, 2007.
- Park, K., Kittelson, D. B., Zachariah, M. R., and Mc-Murry, P. H.: Measurement of inherent material density of nanoparticle agglomerates, J. Nanoparticle Res., 6, 267–272, https://doi.org/10.1023/b:nano.0000034657.71309.e6, 2004.
- Pernov, J. B., Gros-Daillon, J., and Schmale, J.: Comparison of selected surface level ERA5 variables against in-situ observations in the continental Arctic, Q. J. R. Meteorol. Soc., 150, 2123–2146, https://doi.org/10.1002/qj.4700, 2024.
- Petzold, A., Ogren, J. A., Fiebig, M., Laj, P., Li, S.-M., Baltensperger, U., Holzer-Popp, T., Kinne, S., Pappalardo, G., Sugimoto, N., Wehrli, C., Wiedensohler, A., and Zhang, X.-Y.: Recommendations for reporting "black carbon" measurements, Atmos. Chem. Phys., 13, 8365–8379, https://doi.org/10.5194/acp-13-8365-2013, 2013.
- Pileci, R. E., Modini, R. L., Bertò, M., Yuan, J., Corbin, J. C., Marinoni, A., Henzing, B., Moerman, M. M., Putaud, J. P., Spindler, G., Wehner, B., Müller, T., Tuch, T., Trentini, A., Zanatta, M., Baltensperger, U., and Gysel-Beer, M.: Comparison of co-located refractory black carbon (rBC) and elemental carbon (EC) mass concentration measurements during field campaigns at several European sites, Atmos. Meas. Tech., 14, 1379–1403, https://doi.org/10.5194/amt-14-1379-2021, 2021.
- Pokorná, P., Zíková, N., Vodička, P., Lhotka, R., Mbengue, S., Holubová Šmejkalová, A., Riffault, V., Ondráček, J., Schwarz, J., and Ždímal, V.: Chemically speciated mass size distribution, particle density, shape and origin of non-refractory PM₁ measured at a rural background site in central Europe, Atmos. Chem. Phys., 22, 5829–5858, https://doi.org/10.5194/acp-22-5829-2022, 2022.

- Przybylak, R.: The Climate of the Arctic, Springer International Publishing, Cham, https://doi.org/10.1007/978-3-319-21696-6, 2016.
- Quinn, P. K., Stohl, A., Arnold, S., Baklanov, A., Berntsen, T. K., Christensen, J. H., Eckhardt, S., Flanner, M., Klimont, Z., and Korsholm, U. S.: AMAP Assessment 2015: Black carbon and ozone as Arctic climate forcers, ISBN 978-82-7971-092-9, 2015.
- Raatikainen, T., Brus, D., Hyvärinen, A.-P., Svensson, J., Asmi, E., and Lihavainen, H.: Black carbon concentrations and mixing state in the Finnish Arctic, Atmos. Chem. Phys., 15, 10057– 10070, https://doi.org/10.5194/acp-15-10057-2015, 2015.
- Rissler, J., Messing, M. E., Malik, A. I., Nilsson, P. T., Nordin, E. Z., Bohgard, M., Sanati, M., and Pagels, J. H.: Effective Density Characterization of Soot Agglomerates from Various Sources and Comparison to Aggregation Theory, Aerosol Sci. Technol., 47, 792–805, https://doi.org/10.1080/02786826.2013.791381, 2013
- Rissler, J., Nordin, E. Z., Eriksson, A. C., Nilsson, P. T., Frosch, M., Sporre, M. K., Wierzbicka, A., Svenningsson, B., Löndahl, J., Messing, M. E., Sjogren, S., Hemmingsen, J. G., Loft, S., Pagels, J. H., and Swietlicki, E.: Effective Density and Mixing State of Aerosol Particles in a Near-Traffic Urban Environment, Environ. Sci. Technol., 48, 6300–6308, https://doi.org/10.1021/es5000353, 2014.
- Rose, D., Gunthe, S. S., Mikhailov, E., Frank, G. P., Dusek, U., Andreae, M. O., and Pöschl, U.: Calibration and measurement uncertainties of a continuous-flow cloud condensation nuclei counter (DMT-CCNC): CCN activation of ammonium sulfate and sodium chloride aerosol particles in theory and experiment, Atmos. Chem. Phys., 8, 1153–1179, https://doi.org/10.5194/acp-8-1153-2008, 2008.
- Ryu, Y.-H. and Min, S.-K.: Long-term evaluation of atmospheric composition reanalyses from CAMS, TCR-2, and MERRA-2 over South Korea: Insights into applications, implications, and limitations, Atmos. Environ., 246, 118062, https://doi.org/10.1016/j.atmosenv.2020.118062, 2021.
- Saathoff, H., Naumann, K.-H., Schnaiter, M., Schöck, W., Möhler, O., Schurath, U., Weingartner, E., Gysel, M., and Baltensperger, U.: Coating of soot and (NH₄)₂SO₄ particles by ozonolysis products of α-pinene, J. Aerosol Sci., 34, 1297–1321, https://doi.org/10.1016/S0021-8502(03)00364-1, 2003a.
- Saathoff, H., Moehler, O., Schurath, U., Kamm, S., Dippel, B., and Mihelcic, D.: The AIDA soot aerosol characterisation campaign 1999, J. Aerosol Sci., 34, 1277–1296, https://doi.org/10.1016/S0021-8502(03)00363-X, 2003b.
- Saathoff, H., Naumann, K.-H., Möhler, O., Jonsson, Å. M., Hallquist, M., Kiendler-Scharr, A., Mentel, Th. F., Tillmann, R., and Schurath, U.: Temperature dependence of yields of secondary organic aerosols from the ozonolysis of α-pinene and limonene, Atmos. Chem. Phys., 9, 1551–1577, https://doi.org/10.5194/acp-9-1551-2009, 2009.
- Samset, B. H., Myhre, G., Schulz, M., Balkanski, Y., Bauer, S., Berntsen, T. K., Bian, H., Bellouin, N., Diehl, T., Easter, R. C., Ghan, S. J., Iversen, T., Kinne, S., Kirkevåg, A., Lamarque, J.-F., Lin, G., Liu, X., Penner, J. E., Seland, Ø., Skeie, R. B., Stier, P., Takemura, T., Tsigaridis, K., and Zhang, K.: Black carbon vertical profiles strongly affect its radiative forcing uncertainty, Atmos. Chem. Phys., 13, 2423–2434, https://doi.org/10.5194/acp-13-2423-2013, 2013.

- Samset, B. H., Stjern, C. W., Andrews, E., Kahn, R. A., Myhre, G., Schulz, M., and Schuster, G. L.: Aerosol Absorption: Progress Towards Global and Regional Constraints, Curr. Clim. Change Rep., 4, 65–83, https://doi.org/10.1007/s40641-018-0091-4, 2018.
- Schaap, M., van Loon, M., ten Brink, H. M., Dentener, F. J., and Builtjes, P. J. H.: Secondary inorganic aerosol simulations for Europe with special attention to nitrate, Atmos. Chem. Phys., 4, 857–874, https://doi.org/10.5194/acp-4-857-2004, 2004.
- Schacht, J., Heinold, B., Quaas, J., Backman, J., Cherian, R., Ehrlich, A., Herber, A., Huang, W. T. K., Kondo, Y., Massling, A., Sinha, P. R., Weinzierl, B., Zanatta, M., and Tegen, I.: The importance of the representation of air pollution emissions for the modeled distribution and radiative effects of black carbon in the Arctic, Atmos. Chem. Phys., 19, 11159–11183, https://doi.org/10.5194/acp-19-11159-2019, 2019.
- Schnaiter, M., Horvath, H., Möhler, O., Naumann, K.-H., Saathoff, H., and Schöck, O. W.: UV-VIS-NIR spectral optical properties of soot and soot-containing aerosols, J. Aerosol Sci., 34, 1421– 1444, https://doi.org/10.1016/S0021-8502(03)00361-6, 2003.
- Schnaiter, M., Linke, C., Möhler, O., Naumann, K.-H., Saathoff, H., Wagner, R., Schurath, U., and Wehner, B.: Absorption amplification of black carbon internally mixed with secondary organic aerosol, J. Geophys. Res. Atmospheres, 110, https://doi.org/10.1029/2005JD006046, 2005.
- Schnaiter, M., Gimmler, M., Llamas, I., Linke, C., Jäger, C., and Mutschke, H.: Strong spectral dependence of light absorption by organic carbon particles formed by propane combustion, Atmos. Chem. Phys., 6, 2981–2990, https://doi.org/10.5194/acp-6-2981-2006, 2006.
- Schneider, J., Höhler, K., Wagner, R., Saathoff, H., Schnaiter, M., Schorr, T., Steinke, I., Benz, S., Baumgartner, M., Rolf, C., Krämer, M., Leisner, T., and Möhler, O.: High homogeneous freezing onsets of sulfuric acid aerosol at cirrus temperatures, Atmos. Chem. Phys., 21, 14403–14425, https://doi.org/10.5194/acp-21-14403-2021, 2021.
- Schulz, H., Zanatta, M., Bozem, H., Leaitch, W. R., Herber, A. B., Burkart, J., Willis, M. D., Kunkel, D., Hoor, P. M., Abbatt, J. P. D., and Gerdes, R.: High Arctic aircraft measurements characterising black carbon vertical variability in spring and summer, Atmos. Chem. Phys., 19, 2361–2384, https://doi.org/10.5194/acp-19-2361-2019, 2019.
- Schulz, M., Textor, C., Kinne, S., Balkanski, Y., Bauer, S., Berntsen, T., Berglen, T., Boucher, O., Dentener, F., Guibert, S., Isaksen, I. S. A., Iversen, T., Koch, D., Kirkevåg, A., Liu, X., Montanaro, V., Myhre, G., Penner, J. E., Pitari, G., Reddy, S., Seland, Ø., Stier, P., and Takemura, T.: Radiative forcing by aerosols as derived from the AeroCom present-day and pre-industrial simulations, Atmos. Chem. Phys., 6, 5225–5246, https://doi.org/10.5194/acp-6-5225-2006, 2006.
- Schwarz, Joshua. P., Katich, J. M., Lee, S. L., Thomson, D. S., and Watts, L. A.: "Invisible bias" in the single particle soot photometer due to trigger deadtime, Aerosol Sci. Technol., 56, 623–635, https://doi.org/10.1080/02786826.2022.2064265, 2022.
- Sedlacek, A. J., Lewis, E. R., Onasch, T. B., Zuidema, P., Redemann, J., Jaffe, D., and Kleinman, L. I.: Using the Black Carbon Particle Mixing State to Characterize the Lifecycle of Biomass Burning Aerosols, Environ. Sci. Technol., 56, 14315–14325, https://doi.org/10.1021/acs.est.2c03851, 2022.

- Sipkens, T. A., Trivanovic, U., Naseri, A., Bello, O. W., Baldelli, A., Kazemimanesh, M., Bertram, A. K., Kostiuk, L., Corbin, J. C., Olfert, J. S., and Rogak, S. N.: Using two-dimensional distributions to inform the mixing state of soot and salt particles produced in gas flares, J. Aerosol Sci., 158, 105826, https://doi.org/10.1016/j.jaerosci.2021.105826, 2021.
- Sorensen, C. M.: The Mobility of Fractal Aggregates: A Review, Aerosol Sci. Technol., 45, 765–779, https://doi.org/10.1080/02786826.2011.560909, 2011.
- Stephens, M., Turner, N., and Sandberg, J.: Particle identification by laser-induced incandescence in a solid-state laser cavity, Appl. Opt., 42, 3726–3736, https://doi.org/10.1364/AO.42.003726, 2003.
- Tillmann, R., Saathoff, H., Brauers, T., Kiendler-Scharr, A., and Mentel, T. F.: Temperature dependence of the rate coefficient for the α-pinene reaction with ozone in the range between 243 K and 303 K, Phys. Chem. Chem. Phys., 11, 2323, https://doi.org/10.1039/b813407c, 2009.
- Umo, N. S., Ullrich, R., Maters, E. C., Steinke, I., Benker, N., Höhler, K., Wagner, R., Weidler, P. G., Hoshyaripour, G. A., Kiselev, A., Kueppers, U., Kandler, K., Dingwell, D. B., Leisner, T., and Möhler, O.: The Influence of Chemical and Mineral Compositions on the Parameterization of Immersion Freezing by Volcanic Ash Particles, J. Geophys. Res. Atmospheres, 126, e2020JD033356, https://doi.org/10.1029/2020JD033356, 2021.
- Vallon, M., Gao, L., Jiang, F., Krumm, B., Nadolny, J., Song, J., Leisner, T., and Saathoff, H.: LED-based solar simulator to study photochemistry over a wide temperature range in the large simulation chamber AIDA, Atmos. Meas. Tech., 15, 1795–1810, https://doi.org/10.5194/amt-15-1795-2022, 2022.
- Vogel, F.: Short-term Variation in Measurements of Atmospheric Ice-Nucleating Particle Concentrations, PhD Thesis, Karlsruher Institut für Technologie (KIT), 152 pp., https://doi.org/10.5445/IR/1000151147, 2022.
- Vogel, F., Lacher, L., Nadolny, J., Saathoff, H., Leisner, T., and Möhler, O.: Development and validation of a new cloud simulation experiment for lab-based aerosol-cloud studies, Rev. Sci. Instrum., 93, 095106, https://doi.org/10.1063/5.0098777, 2022.
- Wagner, J., Ubele, A. A., Schenzinger, V., and Kreuter, A.: Extended aerosol optical depth (AOD) time series analysis in an Alpine valley: a comparative study from 2007 to 2023, Aerosol Research, 2, 153–159, https://doi.org/10.5194/ar-2-153-2024, 2024.
- Wang, Y., Liu, F., He, C., Bi, L., Cheng, T., Wang, Z., Zhang, H., Zhang, X., Shi, Z., and Li, W.: Fractal Dimensions and Mixing Structures of Soot Particles during Atmospheric Processing, Environ. Sci. Technol. Lett., 4, 487–493, https://doi.org/10.1021/acs.estlett.7b00418, 2017.
- Wang, Y., Ma, P.-L., Peng, J., Zhang, R., Jiang, J. H., Easter, R. C., and Yung, Y. L.: Constraining Aging Processes of Black Carbon in the Community Atmosphere Model Using Environmental Chamber Measurements, J. Adv. Model. Earth Syst., 10, 2514–2526, https://doi.org/10.1029/2018MS001387, 2018.
- Weiss, J. N.: The Hill equation revisited: uses and misuses, FASEB J., 11, 835–841, https://doi.org/10.1096/fasebj.11.11.9285481, 1997.
- Williams, L. R., Gonzalez, L. A., Peck, J., Trimborn, D., McInnis, J., Farrar, M. R., Moore, K. D., Jayne, J. T., Robinson, W. A., Lewis, D. K., Onasch, T. B., Canagaratna, M. R., Trimborn,

- A., Timko, M. T., Magoon, G., Deng, R., Tang, D., de la Rosa Blanco, E., Prévôt, A. S. H., Smith, K. A., and Worsnop, D. R.: Characterization of an aerodynamic lens for transmitting particles greater than 1 micrometer in diameter into the Aerodyne aerosol mass spectrometer, Atmos. Meas. Tech., 6, 3271–3280, https://doi.org/10.5194/amt-6-3271-2013, 2013.
- Willis, M. D., Lee, A. K. Y., Onasch, T. B., Fortner, E. C., Williams, L. R., Lambe, A. T., Worsnop, D. R., and Abbatt, J. P. D.: Collection efficiency of the soot-particle aerosol mass spectrometer (SP-AMS) for internally mixed particulate black carbon, Atmos. Meas. Tech., 7, 4507–4516, https://doi.org/10.5194/amt-7-4507-2014, 2014.
- Wittbom, C., Eriksson, A. C., Rissler, J., Carlsson, J. E., Roldin, P., Nordin, E. Z., Nilsson, P. T., Swietlicki, E., Pagels, J. H., and Svenningsson, B.: Cloud droplet activity changes of soot aerosol upon smog chamber ageing, Atmos. Chem. Phys., 14, 9831–9854, https://doi.org/10.5194/acp-14-9831-2014, 2014.
- Ye, C., Zhang, N., Gao, H., and Zhou, X.: Photolysis of Particulate Nitrate as a Source of HONO and NO_x, Environ. Sci. Technol., 51, 6849–6856, https://doi.org/10.1021/acs.est.7b00387, 2017.
- Yon, J., Bescond, A., and Ouf, F.-X.: A simple semiempirical model for effective density measurements of fractal aggregates, J. Aerosol Sci., 87, 28–37, https://doi.org/10.1016/j.jaerosci.2015.05.003, 2015.
- Yu, C., Pasternak, D., Lee, J., Yang, M., Bell, T., Bower, K., Wu, H., Liu, D., Reed, C., Bauguitte, S., Cliff, S., Trembath, J., Coe, H., and Allan, J. D.: Characterizing the Particle Composition and Cloud Condensation Nuclei from Shipping Emission in Western Europe, Environ. Sci. Technol., 54, 15604–15612, https://doi.org/10.1021/acs.est.0c04039, 2020.
- Yuan, C., Zheng, J., Ma, Y., Jiang, Y., Li, Y., and Wang, Z.: Significant restructuring and light absorption enhancement of black carbon particles by ammonium nitrate coating, Environ. Pollut., 262, 114172, https://doi.org/10.1016/j.envpol.2020.114172, 2020.
- Zanatta, M., Laj, P., Gysel, M., Baltensperger, U., Vratolis, S., Eleftheriadis, K., Kondo, Y., Dubuisson, P., Winiarek, V., Kazadzis, S., Tunved, P., and Jacobi, H.-W.: Effects of mixing state on optical and radiative properties of black carbon in the European Arctic, Atmos. Chem. Phys., 18, 14037–14057, https://doi.org/10.5194/acp-18-14037-2018, 2018.
- Zanatta, M., Bozem, H., Köllner, F., Schneider, J., Kunkel, D., Hoor, P., Faria, J. de, Petzold, A., Bundke, U., Hayden, K., Staebler, R. M., Schulz, H., and Herber, A. B.: Airborne survey of trace gases and aerosols over the Southern Baltic Sea: from clean marine boundary layer to shipping corridor effect, Tellus B Chem. Phys. Meteorol., 72, 1–24, https://doi.org/10.1080/16000889.2019.1695349, 2020.
- Zanatta, M., Herber, A., Jurányi, Z., Eppers, O., Schneider, J., and Schwarz, J. P.: Technical note: Sea salt interference with black carbon quantification in snow samples using the single particle soot photometer, Atmos. Chem. Phys., 21, 9329–9342, https://doi.org/10.5194/acp-21-9329-2021, 2021.
- Zanatta, M., Mertes, S., Jourdan, O., Dupuy, R., Järvinen, E., Schnaiter, M., Eppers, O., Schneider, J., Jurányi, Z., and Herber, A.: Airborne investigation of black carbon interaction with low-level, persistent, mixed-phase clouds in the Arctic summer, Atmos. Chem. Phys., 23, 7955–7973, https://doi.org/10.5194/acp-23-7955-2023, 2023.

- Zanatta, M., Bogert, P., Ginot, P., Hoshyaripour, G., Hu, Y., Laj, P., Linke, C., Möhler, O., Saathoff, H., Schnaiter, M., Umo, N. S., Vogel, F., and Wagner, R.: Dataset for the paper entitled "AIDA Arctic transport experiment part 1: simulation of northward transport and ageing effect on fundamental black carbon properties" by Zanatta et al. (2025), Karlsruhe Institute of Technology [data set], https://doi.org/10.35097/7GH3J1JZABRZKCX9, 2025.
- Zare, A., Romer, P. S., Nguyen, T., Keutsch, F. N., Skog, K., and Cohen, R. C.: A comprehensive organic nitrate chemistry: insights into the lifetime of atmospheric organic nitrates, Atmos. Chem. Phys., 18, 15419–15436, https://doi.org/10.5194/acp-18-15419-2018, 2018.
- Zieger, P., Heslin-Rees, D., Karlsson, L., Koike, M., Modini, R., and Krejci, R.: Black carbon scavenging by low-level Arctic clouds, Nat. Commun., 14, 5488, https://doi.org/10.1038/s41467-023-41221-w, 2023.